

**CALIBRATION OF LOW ENERGY PRODUCTION OF  $^{36}\text{Cl}$   
AND THE CREATION OF AN EXPOSURE AGE CALCULATOR**

by

Robert A. Aumer

Submitted in Partial Fulfillment  
of the Requirements for the Degree of  
Master of Science in Applied Mathematics  
with Specialty in Operations Research and Statistics

New Mexico Institute of Mining and Technology  
Socorro, New Mexico

August, 2010

## ABSTRACT

The *CRONUS-Earth Project* is an NSF funded, national collaboration of geoscientists, whose goal is to refine the methods of using cosmogenic isotopes to date initial exposure of rock formations. One area of concern is the calibration of cosmogenic-isotope production rates. Previous attempts to calibrate the low energy (thermal and epithermal) production of  $^{36}\text{Cl}$  ( $P_f(0)^{36}\text{Cl}$ ) have been made but are inconsistent. This thesis provides an analysis of using a depth profile from Copper Canyon to calibrate  $P_f(0)^{36}\text{Cl}$ . We show that for the Copper Canyon calibration site  $P_f(0)^{36}\text{Cl}$  must be  $1056.2 \pm 110$  ( $\text{n g}^{-1} \text{ yr}^{-1}$ ).

In addition to calibration, we develop a MATLAB based calculator for estimating the exposure ages and erosion rates from depth profiles. We discuss the development of our calculator and provide an example of its functionality with a  $^{10}\text{Be}$  profile from Greenland. Finally, we compare our age and erosion estimates to the published values in Goehring (2010), and show that they are within the uncertainties of each other.

# CONTENTS

<b>LIST OF TABLES</b>	<b>iv</b>
<b>LIST OF FIGURES</b>	<b>v</b>
<b>1. INTRODUCTION</b>	<b>1</b>
1.1 Background . . . . .	1
1.2 Measurement of Nuclide Ratios . . . . .	4
1.3 Scaling Schemes . . . . .	5
1.4 Need for Calibration . . . . .	7
1.5 Age Calculators . . . . .	9
<b>2. PRODUCTION RATE CALIBRATION</b>	<b>11</b>
2.1 Profile Creation . . . . .	11
2.2 Synthetic Calibration . . . . .	16
2.2.1 Choosing a site . . . . .	17
2.2.2 Site Characteristics . . . . .	19
2.2.3 Parameter Estimation . . . . .	19
2.2.4 Calibration . . . . .	22
2.2.5 Results . . . . .	23

2.3	Actual Calibration . . . . .	24
2.3.1	Calibration Summary . . . . .	30
<b>3.</b>	<b>DEPTH PROFILE CALCULATOR</b>	<b>31</b>
3.1	Bayesian Method . . . . .	31
3.1.1	The Posterior Distribution . . . . .	32
3.1.2	Calculator Example . . . . .	35
<b>4.</b>	<b>SUMMARY AND CONCLUSIONS</b>	<b>45</b>
	<b>REFERENCES</b>	<b>47</b>

## LIST OF TABLES

1.1	Notational legend . . . . .	4
1.2	Pf(0) table . . . . .	8
2.1	Synthetic calibration results . . . . .	24
2.2	Calibration summary . . . . .	27
2.3	Calibration summary 2 . . . . .	28
3.1	Greenland results . . . . .	42
3.2	Relative uncertainties . . . . .	42

## LIST OF FIGURES

1.1	Diagram of cosmic bombardment . . . . .	2
2.1	Production vs. depth . . . . .	11
2.2	Depth concentration profiles for an erosion rate of zero . . . . .	15
2.3	Depth concentration profiles for an erosion rate of 5 mm / 1000 years	16
2.4	Erosion rate vs. equilibrium age . . . . .	18
2.5	Copper Canyon site schematic . . . . .	20
2.6	Relative Cl-36 production rates for the Copper Canyon calibration site . . . . .	21
2.7	Production rate–erosion rate trade off . . . . .	22
2.8	$\chi^2$ hyper-surface of the synthetic calibration . . . . .	25
2.9	Synthetically calibrated chlorine-36 profile . . . . .	25
2.10	Synthetically calibrated beryllium-10 profile . . . . .	26
2.11	Actual calibration $\chi^2$ hyper-surface . . . . .	26
2.12	Calibrated beryllium-36 profile . . . . .	28
2.13	Calibrated chlorine-36 profile . . . . .	29
2.14	Residuals plot . . . . .	29
3.1	Marginal distribution for erosion rate . . . . .	37

3.2	Marginal distribution for age . . . . .	38
3.3	Marginal distribution for inheritance . . . . .	38
3.4	Joint posterior marginalized over inheritance . . . . .	39
3.5	Joint posterior marginalized over erosion rate . . . . .	40
3.6	Joint posterior marginalized over age . . . . .	40
3.7	Greenland profile . . . . .	43
3.8	Greenland profile 2 . . . . .	44

This thesis is accepted on behalf of the faculty of the Institute by the following committee:

---

Brian Borchers, Advisor

---

---

---

---

I release this document to the New Mexico Institute of Mining and Technology.

---

Robert A. Aumer

Date

# CHAPTER 1

## INTRODUCTION

### 1.1 Background

Terrestrial cosmogenic nuclide (TCN) dating is a technique used in the field of geochronology to date the initial exposure of rock surfaces. The technique relies upon measuring concentrations of a handful of nuclides. The most common nuclides used are  $^3\text{He}$ ,  $^{10}\text{Be}$ ,  $^{14}\text{C}$ ,  $^{21}\text{Ne}$ ,  $^{26}\text{Al}$ , and  $^{36}\text{Cl}$  (Gosse and Phillips, 2001). The production of these TCNs are a result of nuclear reactions, which originate from bombarding cosmic radiation.

Throughout history, the explosions of supernovae have supplied the earth with a near constant source of cosmic radiation (Dunai, 2010). Primarily, the radiation is in the form of high energy protons and  $\alpha$ -particles (Dunai, 2010). The interaction of these particles with the atmosphere creates a cascade of neutrons and muons, which then collide with the earth's surface. When the barrage of neutrons reaches exposed terrestrial rocks, further nuclear reactions occur that produce the TCNs of interest. A simplified diagram is given in figure 1.1. By measuring these TCNs and using reliable nuclide production rates and accurate production models, geologists can calculate a surface exposure age. Next, we will discuss TCN production in more detail.

Specifically, there are three pathways in which TCNs are produced; (i) high energy neutron spallation, (ii) low energy (thermal and epithermal) neutron ab-

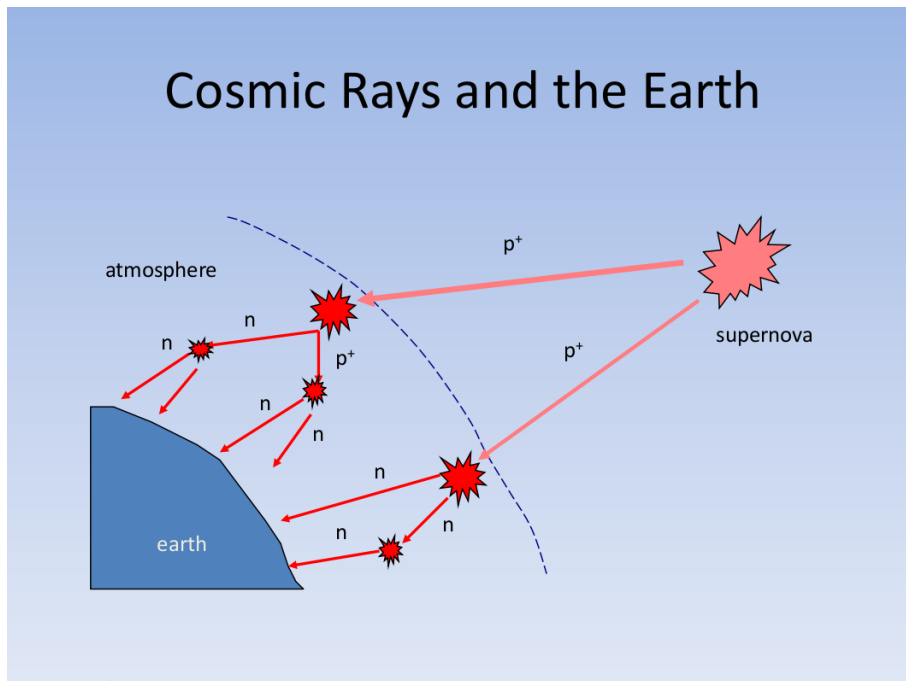


**Figure 1.1:** Diagram of cosmic bombardment. The diagram shows the primary source of radiation, protons ( $p^+$ ), reacting in the atmosphere to create a cascade of secondary particles, neutrons ( $n$ ), which then collide with the Earth's surface (Marrero, 2009).

sorption, and (iii) fast and slow muon capture. The high energy neutrons collide with terrestrial minerals, causing certain atoms to spall some protons and neutrons. The result is the formation of new, lower atomic number nuclides. For example, the high energy spallation of  $^{40}\text{Ca}$  loses nucleons to form  $^{36}\text{Cl}$ . The rate at which these spallation reactions occur decreases exponentially with depth. Lower energy neutrons, including the newly liberated neutrons via spallation, are absorbed by surrounding minerals in a diffusive manner as described in Phillips (2001). Lastly there is also muonic production of TCNs, which is described in Heisinger (2002). Not every TCN is produced by all three pathways. Production of  $^{10}\text{Be}$  for instance, is created only from spallation and muon capture.  $^{36}\text{Cl}$  on the other hand, is produced by all 3 pathways. To avoid the confusion of outlining particular pathways for each TCN, we will instead describe all three pathways once, in terms of  $^{36}\text{Cl}$ .

The main players in  $^{36}\text{Cl}$  production are from calcium, potassium and chlorine.  $^{40}\text{Ca}$  and  $^{39}\text{K}$  are responsible for the majority of  $^{36}\text{Cl}$  produced by spallation and muons. However  $^{47}\text{Ti}$  and  $^{55}\text{Fe}$  also produce  $^{36}\text{Cl}$  by spallation and muons but are much less significant.  $^{36}\text{Cl}$  production from thermal and epithermal neutrons is exclusively from  $^{35}\text{Cl}$ . For convenience we will use the same notation for TCN production that is presented in the Gosse and Phillips (2001) overview of the subject.  $P_{n,m}^{36}\text{Cl}$  denotes the production of  $^{36}\text{Cl}$  from nuclide  $m$  by pathway  $n$ . Table 1.1 lists the pathways relevant to this paper. For the purpose of this thesis, it is sufficient for the reader to simply be aware of these pathways. It is not necessary to understand the nuclear physics in detail.

Pathway	Notation
Spallation	$s$
Muonic	$\mu$
Thermal	th
Epithermal	eth

**Table 1.1:** Notational legend taken from Gosse and Phillips (2001)

## 1.2 Measurement of Nuclide Ratios

After appropriate samples have been collected, they can be processed in two ways: whole rock and mineral separates. Whole rock samples may be composed of many different minerals. Researchers have to measure the amount of TCN-producing material within the sample. The more rigorous technique of mineral separate involves mechanical processes, in which the whole rock is broken down into its constituent minerals. The mineral separates technique provides more meaningful data as it isolates just one reaction pathway. In either case, isotope dilution mass spectrometry (IDMS) techniques are used to determine the amount of target nuclide that is present.

For either sampling technique, the processing generally follows the same procedures. Specifically for  $^{36}\text{Cl}$  the processing goes as follows. First, a sample is crushed, leached in acid, and sent to the X-ray Fluorescence (XRF) lab to determine the bulk rock composition. Once compositional results are received, the sample is then spiked with purified chloride of a precisely known volume and isotope ratio  $(^{35}\text{Cl}/^{37}\text{Cl})_{\text{known}}$ . To ensure the accuracy of the dilution process it is important that spike have a ratio of  $(^{35}\text{Cl}/^{37}\text{Cl}) > 10$  (Desilets et al., 2006a). The sample is then dissolved and further chemically processed to clean and purify the target element. Next, the sample is run through a mass accelerator that measure

two ratios,  $(^{36}\text{Cl}/^{35}\text{Cl})_{\text{meas}}$  and  $(^{35}\text{Cl}/^{37}\text{Cl})_{\text{meas}}$ . From these two ratios, and

$$[\text{Cl}_{\text{rck}}] = \left[ \frac{\left(\frac{^{35}\text{Cl}}{^{37}\text{Cl}}\right)_{\text{meas}} [^{37}\text{Cl}_{\text{spk}}] - [^{35}\text{Cl}_{\text{spk}}]}{\left(\frac{^{35}\text{Cl}}{^{37}\text{Cl}}\right)_{\text{rck}} - \left(\frac{^{35}\text{Cl}}{^{37}\text{Cl}}\right)_{\text{meas}}} \right] \cdot \left[ 1 + \left(\frac{^{35}\text{Cl}}{^{37}\text{Cl}}\right)_{\text{rck}} \right] \quad (1.1)$$

$$\left(\frac{^{36}\text{Cl}}{\text{Cl}}\right)_{\text{meas}} = \frac{[^{36}\text{Cl}_{\text{rck}}]}{[^{37}\text{Cl}_{\text{rck}}] + [^{37}\text{Cl}_{\text{spk}}] + [^{36}\text{Cl}_{\text{rck}}] + [^{36}\text{Cl}_{\text{spk}}]} \quad (1.2)$$

we obtain how much  $^{36}\text{Cl}$  is in the rock with

$$\left(\frac{^{36}\text{Cl}}{\text{Cl}}\right)_{\text{rck}} = \left(\frac{^{36}\text{Cl}}{\text{Cl}}\right)_{\text{meas}} \cdot \left[ 1 + \frac{[\text{Cl}_{\text{spk}}]}{[\text{Cl}_{\text{rck}}]} \right]. \quad (1.3)$$

By comparing the difference between the measured (S/S) and the spiking agent, we are able to back-calculate the isotope concentration in atoms of  $^{36}\text{Cl}$  per total Cl atoms (Desilets et al., 2006a).

The last step is to blank correct each sample. During lab processing, a blank is created to correct for chlorine and  $^{36}\text{Cl}$  added during the chemical processing. A blank correction is performed for the  $^{36}\text{Cl}$  contribution (on a per sample basis) as well as the total chloride in the sample. Total chloride is assumed to be contributed through the addition of reagents to the samples and is subtracted based on total amount of reagent added. A similar approach is used for measuring  $^{10}\text{Be}$ ,  $^{26}\text{Al}$ , and other nuclides, with the only marked differences being the carrier and spiking solutions.

### 1.3 Scaling Schemes

The basic idea behind TCN dating is, if we know the rate of TCN production, we can theoretically calculate the age of the rock sample based on how much nuclide is present. The reality is that there are many factors controlling the

nuclide production rates. Scaling for these factors proves to be one of the most challenging aspects of the TCN process. These factors, to name a few, include latitude, atmospheric pressure/elevation, terrain shielding, and temporal variations in the geomagnetic field. Thus for production rates to be useful globally, scaling schemes must be in place to normalize rates to a reference time and location. At high latitudes the magnetic field is nearly parallel to incoming particles, thus variations in field strength have little effect on production rates. Altitude, or more precisely barometric pressure, must also be scaled for each sample. Simply put, the more atmosphere over head, the less cosmic-ray flux will be reaching the surface. Thus, production rates at any arbitrary location are scaled, using high latitude sea-level (HLSL) production rates as a baseline.

Our standardized production rates also assume that a sample has been exposed to cosmic radiation with 360 degrees of unobstructed view of the horizon. When an obstruction is present, such as a mountain or canyon wall, we must scale back production at that site due to the blocking of low angle cosmic rays. Terrain scaling is done on site-by-site basis.

A few scaling schemes have been modeled after neutron monitor observations (Dunai, 2001),(Desilets et al., 2006b),and (Lifton et al., 2005), while others rely on analytical results (Sato et al., 2008),(Sato and Niita, 2006). Next, we address the specific issues with the various individual scaling schemes.

The original and most commonly cited scaling scheme was developed by Lal (1991), which for mid to high latitudes seems to accurately scale spallogenic production rate variation due to altitude and latitude. However, the simplicity of the model has one key flaw, the lack of time dependency. It is well established that the earth's magnetic field, which influences TCN production, has varied over

time. Lal's produces a constant production rate by assuming the Earth's magnetic field strength is constant. Stone et al. (2000) makes a slight amendment to Lal's scheme by scaling for atmospheric pressure instead of altitude. This modification better describes the mechanism responsible for the production rate variation but still lacks time dependence.

The measure of appropriateness of a scaling model can be tested simply by how well it can produce accurate production rates given any sample location. In Balco (2007), five different scaling schemes were compared using  $^{10}\text{Be}/^{26}\text{Al}$  data. They included the Lal/Stone, Desilets (2006), Dunai (2001), Lifton et al. (2005) schemes, and a fifth scheme combining the Lal/Stone with a time dependent magnetic field component from Nishiizumi (Lal, 1991),(Desilets et al., 2006b), (Dunai, 2001), (Lifton et al., 2005),(Nishiizumi et al., 1989). The five schemes were compared using a single calibration set. The results of that work showed that actually none of the five schemes fit the calibration data to an acceptable degree of errors (Balco et al., 2008).

Recently, N.A. Lifton, Purdue University (pers. comm, 2011) has put together a scaling scheme that is essentially the Lifton (2005) scheme, with neutron flux calculations taken directly from Sato (2006) Lifton (pers. comm, 2011). While not yet published, the latest production rate calibration results suggest that the Lifton/Sato scaling is better fitting any previous scaling scheme. All computations presented in this thesis were done using the Lifton/Sato scheme.

#### **1.4 Need for Calibration**

Accuracy and reproducibility problems have been acknowledged by the TCN dating community. Two of the main goals of CRONUS are to achieve the

discipline-wide reproducibility of results and to eliminate systematic errors as much as possible. These goals will be met in part by the proper calibration of each of the TCN production rates. Central to this thesis is the improvement in the precision and accuracy of the estimated  $^{36}\text{Cl}$  production rate via thermal and epithermal pathways ( $P_i(0)^{36}\text{Cl}$ ).

There are three main sources for  $^{36}\text{Cl}$  production rates in the literature: (Phillips et al., 2001), (Evans, 2001), and (Swanson and Caffee, 2001). Table 1.2 summarizes the  $P_i(0)^{36}\text{Cl}$  estimates of the 3 authors. In Marrero (2009), the three

$P_i(0)^{36}\text{Cl}$	$\pm 1\sigma$	Author
626	105	(Phillips et al., 2001)
726	28	(Evans, 2001)
740	63	(Swanson and Caffee, 2001)

**Table 1.2:** Table of  $P_i(0)$  estimates.

sets of production rates are compared using two independently dated sites: Promontory Point (PPT) and Tabernacle Hill (TAB). Using CHLOE, a spreadsheet style calculator, each author's production rates were used to date both the PPT and TAB sites (Marrero, 2009). Marrero showed that while the Phillips (2001) production rates fit best (i.e. smallest reduced  $\chi^2_v$ ), none of the three production rate sets fit adequately to both sites (Marrero, 2009). Marrero (2009) also points out the inherent sensitivity of a production-rate estimate to the assumed erosion rate, and suggests using depth profile calibration as a remedy.

Other unpublished attempts to calibrate  $P_i(0)^{36}\text{Cl}$  have been made by the New Mexico Tech group. The two main spallation production rates ( $P_{s,K}^{36}\text{Cl}$ ,  $P_{s,Ca}^{36}\text{Cl}$ ) and  $P_i(0)^{36}\text{Cl}$  were simultaneously fitted from CRONUS Earth's global calibration data set Borchers (pers. comm, 2011). Calibrations of this nature have shown that

estimates for both  $P_{s,K}^{36}\text{Cl}$  and  $P_{s,Ca}^{36}\text{Cl}$  are both strongly inversely correlated with the estimate of  $P_f(0)^{36}\text{Cl}$ . Thus equally acceptable fits can be obtained by increasing either  $P_{s,K}^{36}\text{Cl}$  or  $P_{s,Ca}^{36}\text{Cl}$  and decreasing  $P_f(0)^{36}\text{Cl}$ . Similarly, one can also decrease either spallation rates and increase  $P_f(0)^{36}\text{Cl}$  and get equally good fits. There are two possible ways to remedy this problem. Expanding the calibration data to include many more combinations of production from the 3 pathways might help resolve the correlation issue. Alternatively one could try to independently constrain one of the highly correlated parameters, which would in turn constrain the corresponding correlated parameters. In chapter 2 we will discuss our attempt to resolve  $P_f(0)^{36}\text{Cl}$  using depth profile calibration, as suggested in Marrero (2009).

## 1.5 Age Calculators

Once satisfied with the calibrated production rates, CRONUS must also provide consistent ways for scientists to perform cosmogenic dating.

Greg Balco and others developed an online  $^{10}\text{Be}/^{26}\text{Al}$  calculator (Balco et al., 2008). Balco's work provides a standard method and internally consistent dating results from surface  $^{10}\text{Be}$  and  $^{26}\text{Al}$  measurements. The calculator also provides a forum to compare sample sets using the various available scaling schemes. Work such as this is vital to the development and improvement of new and existing scaling schemes (Balco et al., 2008).

Currently, most available calculators are nuclide specific. It is more desirable, however, to have a general calculator—one which is applicable, and internally consistent, for all the popular TCNs. Shasta Marrero and others, have put together a surface age-calculator for a multitude of TCNs ( $^{36}\text{Cl}$ ,  $^{10}\text{Be}/^{26}\text{Al}$ , and  $^{14}\text{C}$ ). Like Balco's, Marrero's calculator can use any of the historical scaling schemes, as

well as the newly developed Lifton/Sato. Another useful aspect of the Marrero calculator is its modular design. As scaling schemes and production models are refined, they can easily be incorporated into the code.

While Marreo's calculator multi-nuclide capability is a step in the right direction, it still lacks the ability to date depth profiles. Dating via depth profiles is important because they allow for simultaneous estimation of erosion rate. One calculator that does have the capability to handle depth profiles, is described in Hidy et al. (2010). Presented is a Monte-Carlo style depth-profile age calculator, capable of using  $^{10}\text{Be}/^{26}\text{Al}$ , with the potential for more nuclides once the production models are implemented (Hidy et al., 2010). However, due to Hidy's incorrectly computed posterior distributions, his results should not be trusted. Thus, to date, CRONUS does not yet have the robust, and internally consistent depth-profile calculator it needs.

In chapter 3, we present an extension of the Marrero calculator adapted for depth profiles. And, just like its surface sample counterpart, the depth profile calculator will have versions for a multitude of nuclides. Currently we have a version for  $^{36}\text{Cl}$  and for the commonly paired  $^{10}\text{Be}/^{26}\text{Al}$ . Additional versions will be created as each new nuclide model is adapted for depth.

## CHAPTER 2

### PRODUCTION RATE CALIBRATION

#### 2.1 Profile Creation

Of particular interest in this thesis is the depth-varying production of TCNs. Figure 2.1 shows the production from the different pathways and the change with depth. In this particular sample  $^{36}\text{Cl}$  production is about half from spallation and half from thermal absorption. In general, the relative production between pathways depends upon the composition.

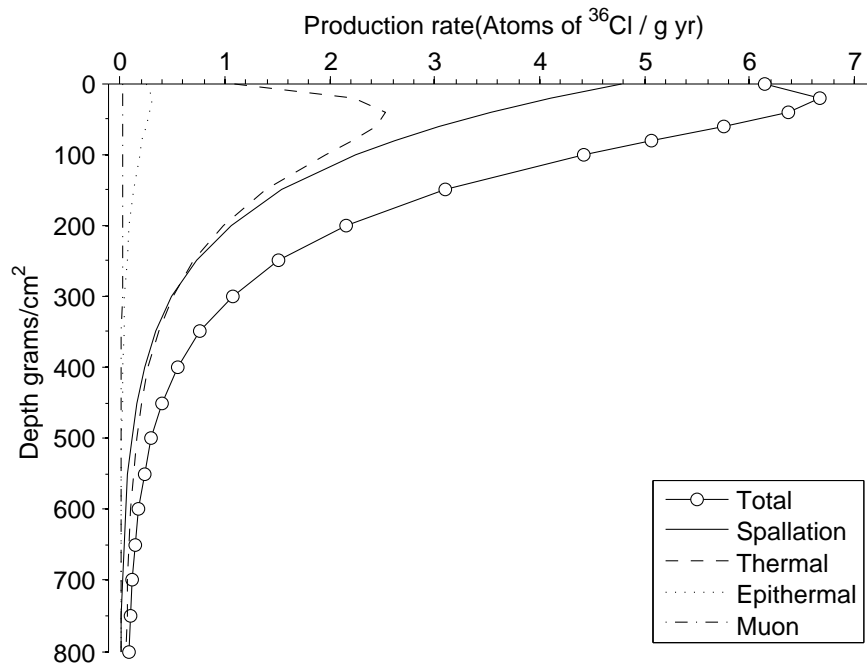


**Figure 2.1:** Production vs. depth. For an arbitrary sample composition, this plot shows how production rate varies with depth for the different pathways.

Our effort to calibrate  $P_f(0)^{36}\text{Cl}$  will utilize depth profiling. In other words, multiple samples at a single location, varying by depth. By using samples that are all from the same location, we rid our calibration of additional sources of error from any inaccuracies the scaling schemes may possess. Fitting measured to predicted concentrations, while adjusting the parameter  $P_f(0)^{36}\text{Cl}$ , the depth profiles become our means of calibration. Before going into detail about the calibration process, we'll explain how the concentration of cosmogenic  $^{36}\text{Cl}$  accumulates to form these profiles.

Depth profiles are the result of two competing processes—(i) production from the cosmogenic radiation, and the (ii) natural decay of radioactive isotopes. At a particular depth and time, the concentration of cosmogenic  $^{36}\text{Cl}$  is given by the solution to eq 2.1,

$$\frac{dc}{dt} = -r \cdot c(t) + P(z(t), s(t)) \quad (2.1)$$

Where  $r$  is the radioactive decay rate of  $^{36}\text{Cl}$  and  $c(t)$  is the concentration of  $^{36}\text{Cl}$  at time  $t$ .  $P(z(t), s(t))$  is the  $^{36}\text{Cl}$  production rate and is implicitly time dependent in two ways,  $z(t)$  and  $s(t)$ . The depth of a sample  $z(t)$  depends on  $t$  because of the erosion rate. For example, consider a sample which at the present is at a depth of 100 mm. Furthermore, suppose that the formation we are sampling from has experienced surface erosion at the rate of 1 mm per thousand years subsequent to exposure. Then if the formation had been exposed 10,000 years ago, that same sample has been exposed to cosmic radiation at depths varying from 100-110 mm. The second way in which production rates vary with time is due to changes in the magnetic field strength over the exposure history of the sample.  $s(t)$  is a time dependent production scaling factor for magnetic field fluctuation.

For clarity in equation 2.1, we presented the production rate  $P$  simply as a function of time-dependent depth-to-sample, and time-dependent scaling. The

actual functional form of  $P = P_{s,m} + P_{eth,m} + P_{th,m} + P_{\mu}$  is the sum of the production from all pathways.  $P$  is given explicitly by the sum of equations 2.2, 2.3, 2.4, and the heisinger muon model (Heisinger et al., 2002). Details on the various parameters can be found in Gosse and Phillips (2001).

$$P_{s,m}(z) = \Psi_{m,k}(0)C_k \exp\left(-\frac{z}{\Lambda_f}\right) \quad (2.2)$$

$$\begin{aligned} P_{eth,m}(z) = & \frac{f_{eth}\Phi_{eth,ss,total}}{\Lambda_{eth,ss}} = \frac{f_{eth}}{\Lambda_{eth,ss}} \left\{ \Phi_{eth,ss}^* \exp\left(-\frac{z}{\Lambda_f}\right) \right. \\ & + (1 + R_{\mu}R_{eth})(F\Delta\Phi)_{eth,ss}^* \exp\left(-\frac{z}{L_{eth,ss}}\right) \\ & \left. + R_{\mu}\Phi_{eth,ss}^* \exp\left(-\frac{z}{\Lambda_{\mu}}\right) \right\} \quad (2.3) \end{aligned}$$

$$\begin{aligned} P_{th,m}(z) = & \frac{f_{th}\Phi_{th,ss,total}}{\Lambda_{th,ss}} = \frac{f_{th}}{\Lambda_{th,ss}} \left\{ \Phi_{th,ss}^* \exp\left(-\frac{z}{\Lambda_f}\right) \right. \\ & + (1 + R'_{\mu})(\Im\Delta\Phi)_{eth,ss}^* \exp\left(-\frac{z}{L_{eth,ss}}\right) \\ & + (1 + R'_{\mu}R_{th})(\Im\Delta\Phi)_{th,ss}^* \exp\left(-\frac{z}{L_{eth,ss}}\right) \\ & \left. + R'_{\mu}\Phi_{th,ss}^* \exp\left(-\frac{z}{\Lambda_{\mu}}\right) \right\} \quad (2.4) \end{aligned}$$

There is also the issue of inheritance. Whenever dating the exposure of a sedimentary feature, we must consider the likelihood that the parent material had already contained  $^{36}\text{Cl}$  during deposition. The additional  $^{36}\text{Cl}$ , minus that which would have decayed in the time between deposition and exposure, we call the sample's inherited  $^{36}\text{Cl}$ . This amount makes up the initial conditions of equation

2.1.  $c(o) = c_0$  or zero in the case of no inheritance. When displaying results, we'll unitize inheritance as equivalent years of exposure at current production rates. Because of the overall complexities of the model, in practice we calculate concentrations by numerically integrating equation 2.1.

For any given age  $t^*$  and vector of depths  $z$ , the solution  $c(t^*)$  gives us a  $^{36}\text{Cl}$  concentration depth profile. For the spallation pathways, Equation 2.1 had solutions that are very nearly exponential. For neutron capture at thermal and epithermal energy levels, the solutions differ. The flow of neutrons and the subsequent capture by  $^{35}\text{Cl}$  act in a diffusive manner, not unlike heat flow. Neutrons near the free boundary of the rock surface escape to the atmosphere, and no longer have the opportunity to react with terrestrial material. The net effect is a loss of would-be  $^{36}\text{Cl}$  at and near the surface. The resulting solutions form a "hooked exponential" profile. Figure 2.2 shows the  $^{36}\text{Cl}$  profile progression through time, in the presence of zero erosion. The lower 2/3 of the profile looks practically exponential. However at the surface we see the effect of the free boundary has on the low energy neutron flux.

Something else to notice is that these profiles reach an equilibrium somewhere in the vicinity of 2 million years. This phenomenon is both an expected and welcome result. For a very old sample, age becomes a non factor to the shape and location of the profile. So as long as an equilibrated sample is used in the calibration when can ignore the samples age, thus relieving us of one more parameter to estimate. Next we'll discuss the progression in figure 2.3. In this figure we see that at a higher erosion rate (5 mm per 1000 years), the hook has completely vanished. It is apparent that removing the top layers of rock through erosion can effectively erase evidence of the hook. Even more important is the difference in

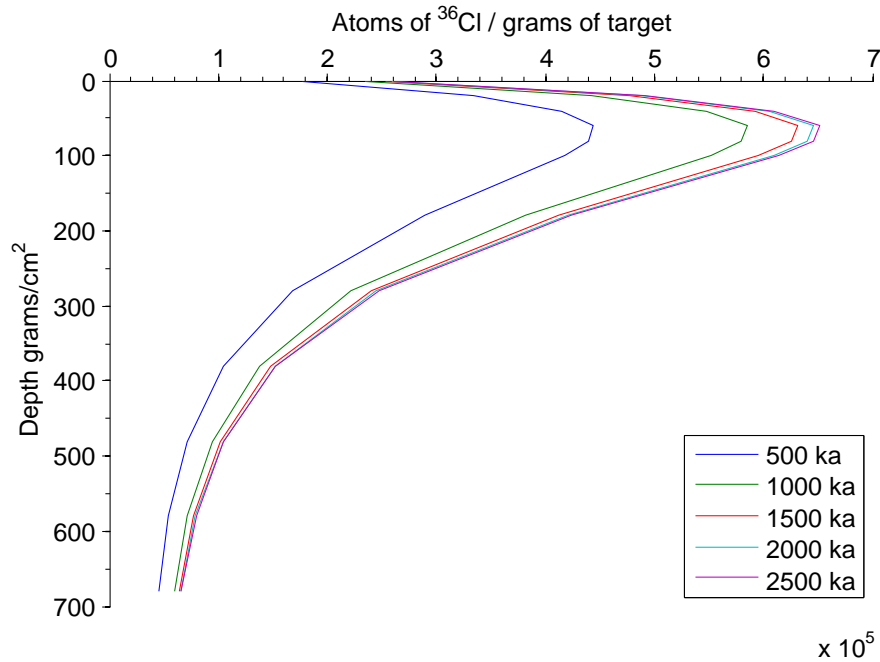


**Figure 2.2:** Depth concentration profiles for an erosion rate of zero. The figure shows the build up of a Cl-36 profile over time

the equilibrium age between the two cases. In the presence of a higher erosion rate the length of time for a sample to reach equilibrium decreases, along with the equilibrium concentration. The implications of not knowing the erosion rates are great. For example, suppose we are looking at a profile like that of the youngest (left most) profile under zero erosion. Further suppose the resolution of the data is such that one cannot determine with certainty whether or not a hook exists. Now compare that theoretical profile to an equilibrated profile in figure 2.3. Without knowledge of the hook, the two profiles would be essentially indistinguishable. Therefore without knowledge of the erosion rate we cannot hope to proceed with calibration. The only solution is to simultaneously estimate erosion along side  $P_i(0)^{36}\text{Cl}$ . Muonic production curves are different still, and are only approximately exponential. Our calculation of muon production with depth is a direct adaptation of the muon systematics of Heisinger et al. (2002), with depth scaling

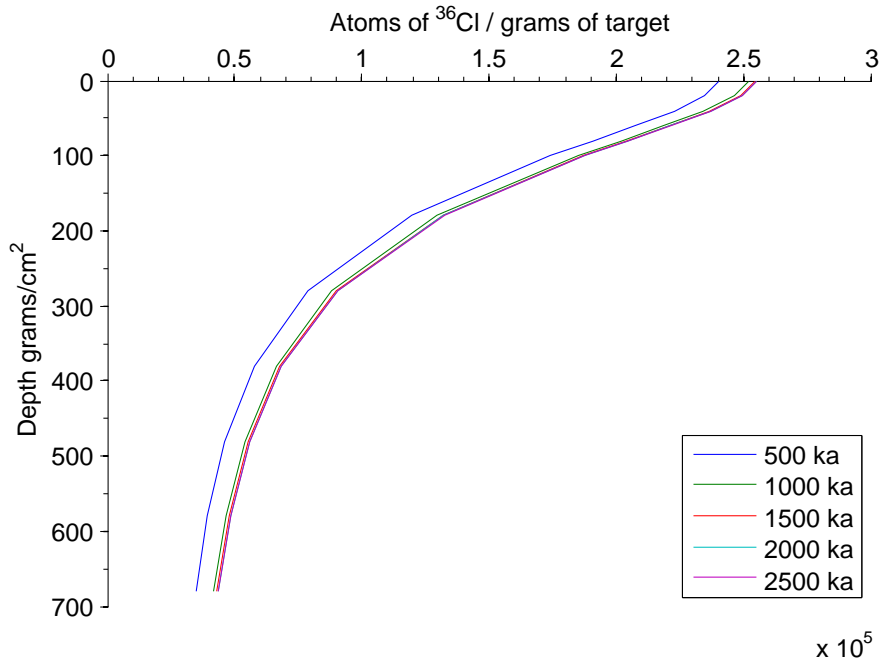


**Figure 2.3:** Depth concentration profiles for an erosion rate of 5 mm / 1000 years. The figure shows the build up of a Cl-36 profile over time

of the muon fluxes from Sato et al. (2008) Lifton (pers. comm, 2011).

## 2.2 Synthetic Calibration

By sampling via depth profiles, it may be possible to increase the accuracy of the published  $P_f(0)^{36}\text{Cl}$  production rate. Of course the accuracy depends on how much information we can extract from a calibration sample. It is to our benefit to predetermine what site characteristics will optimize calibration exercise, not only for the goal of accuracy but the expedience of the project. Using synthetic examples we simulated different hypothetical sampling site characteristics and determined both the necessary conditions for proper calibration, and how well we expect to do with ideal conditions. It is important to point out that experimenting with synthetic examples relies entirely on the correctness of our

modeling. Thus, our synthetic results can only provide an lower bound on the error of the calibration.

### 2.2.1 Choosing a site

From the first swing of the rock hammer, to the finished results returning from the accelerator, the time it takes to obtain a complete depth profile is measured in months. Additionally, the high cost of the chemical and accelerator processing make site selection critical. When considering a site for calibration, we must have a suitable mineral composition for which low energy production is dominant. But because of the high cost of obtaining a profile, it is in the best interest of the project to select a site from which we can harvest the most information. Next we determine the preferred sample site characteristics, and discuss the sensitivity of our calibration to different scenarios.

A characteristic that a site must have is old age. More specifically, it must have been exposed long enough ago for the concentration profile of  $^{36}\text{Cl}$  to have reached equilibrium. This was briefly touched upon in the previous section, but now we will go into more detail about our determination of what is old enough. Three competing rates determine the time it takes for a profile to reach equilibrium—production, decay and erosion. The decay rate for  $^{36}\text{Cl}$  is well known and fixed within our calibration. But, how much if any effect does the erosion rate have on the time to equilibrium? Using our production model, depth profiles were created over a range of erosion rates and ages. A constant composition was used, with no inherited chlorine. Figure 2.4 shows the percent change in concentration through time, under different erosion rates. An arbitrary threshold is shown at 1% by the dashed line. We can see from figure 2.4 that the lower the

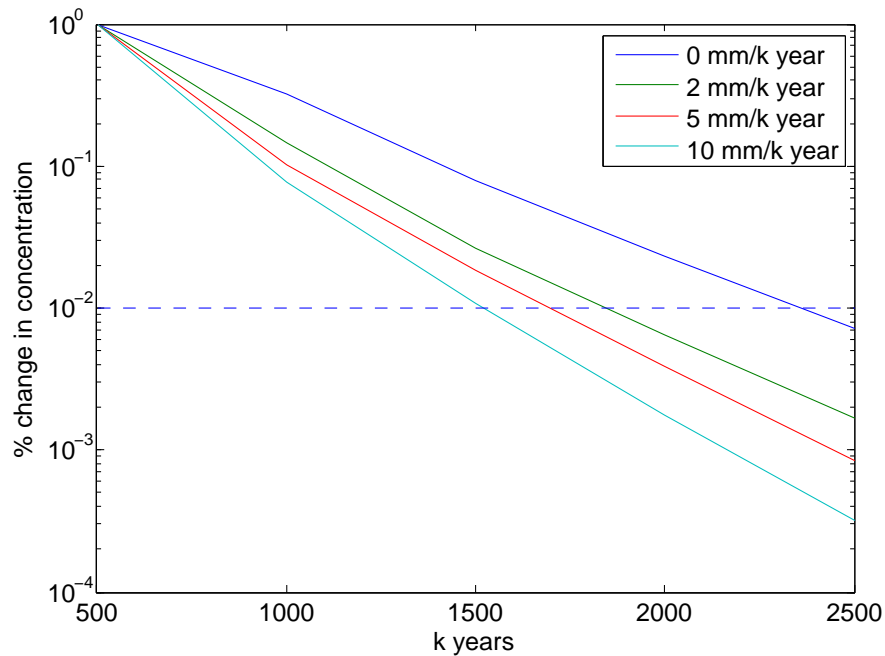


**Figure 2.4:** Erosion rate vs. equilibrium age. For different erosion rates, the change in concentration is plotted against profile age. Also shown is an arbitrary reference line at 1%

erosion rate is, the longer it takes a given profile to reach equilibrium. This is an important result because, as explained in the previous section, high erosion rates mask the profiles hook, making calibration exceedingly difficult. We would prefer a site with low erosion which we now know will have to be much older.

With the necessary calibration conditions in mind (i.e. lower erosion rates and long-exposed rock), our next objective is to determine whether or not the proposed sampling site at Copper Canyon, New Mexico will be suitable for such a calibration. We will also simulate ideal conditions, and determine the feasibility of calibration in the best case. Synthetic data was generated and the calibration was done numerically with code written in Matlab.

### 2.2.2 Site Characteristics

The Copper Canyon mine is located within the Cibola National Forest just southeast of Magdalena, New Mexico. The site is an vertical pit dug into bedrock—approximately 2.5 m deep. The surface topography is a fairly planar hill side which dips approximately  $30^\circ$  to the south. Figure 2.5 shows roughly the pit dimensions and orientation. The site is compositionally suitable for  $P_f(0)^{36}\text{Cl}$  calibration due to the availability of  $^{35}\text{Cl}$ , and the relatively low concentrations of Ca, K, Ti, and Fe—i.e. little production from spallation and muons. Figure 2.6 shows the relative production rates at depth for the Copper Canyon composition. Indeed, the production is dominated by thermal and epithermal production, which make up 91.5% of the total production. The remaining production is from spallation and muons, at 8.39% and 0.11% respectively.

### 2.2.3 Parameter Estimation

The calibration requires us to estimate two unknown parameters— $P_f(0)^{36}\text{Cl}$ , and the erosion rate. Unfortunately there exists a high correlation between  $P_f(0)^{36}\text{Cl}$ , and the erosion rate. Figure 2.7 shows the  $\chi^2$  hyper-surface from attempting to fit both erosion rate and  $P_f(0)^{36}\text{Cl}$  from a single  $^{36}\text{Cl}$  profile. The bold contour represents the 68% confidence region. The problem is that small errors in estimating the erosion rate translate into quite large errors in  $P_f(0)^{36}\text{Cl}$ . In fact figure 2.7 suggests a interval half width of 16%. To defeat this, it has been suggested we use a well established and tightly constrained  $P_{s,\text{SiO}_2}^{10}\text{Be}$  profile along side the  $P_f(0)^{36}\text{Cl}$  Profile, to aid in the erosion rate estimation. By simultaneously fitting both profiles, we hope to be able to tightly constrain  $P_f(0)^{36}\text{Cl}$ .

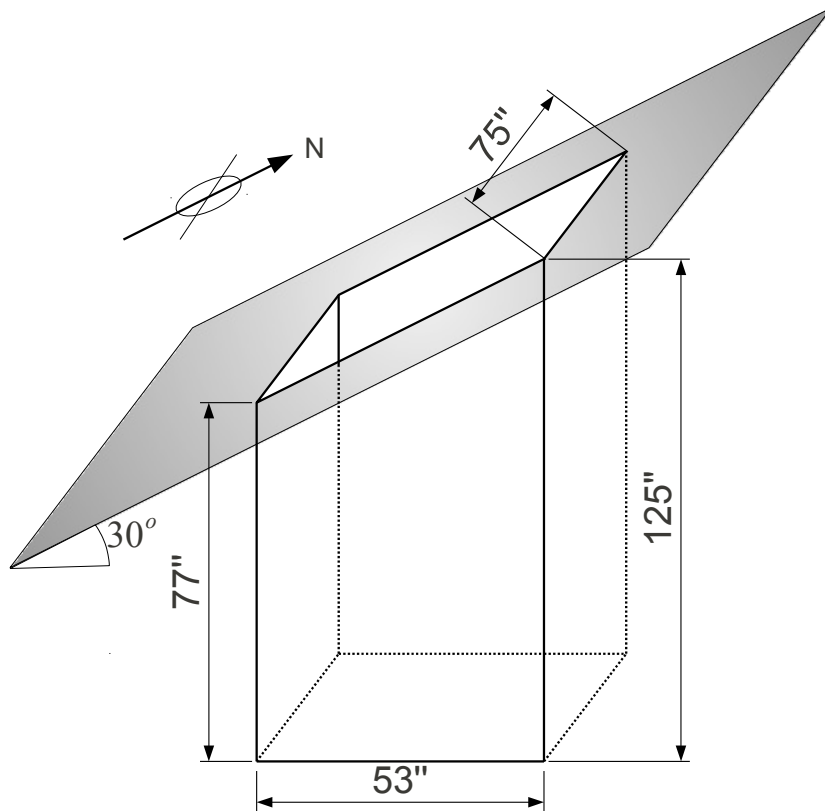


**Figure 2.5:** Shown is a schematic of the open pit at the Copper Canyon calibration site. The depth samples were taken from the east facing pit wall.

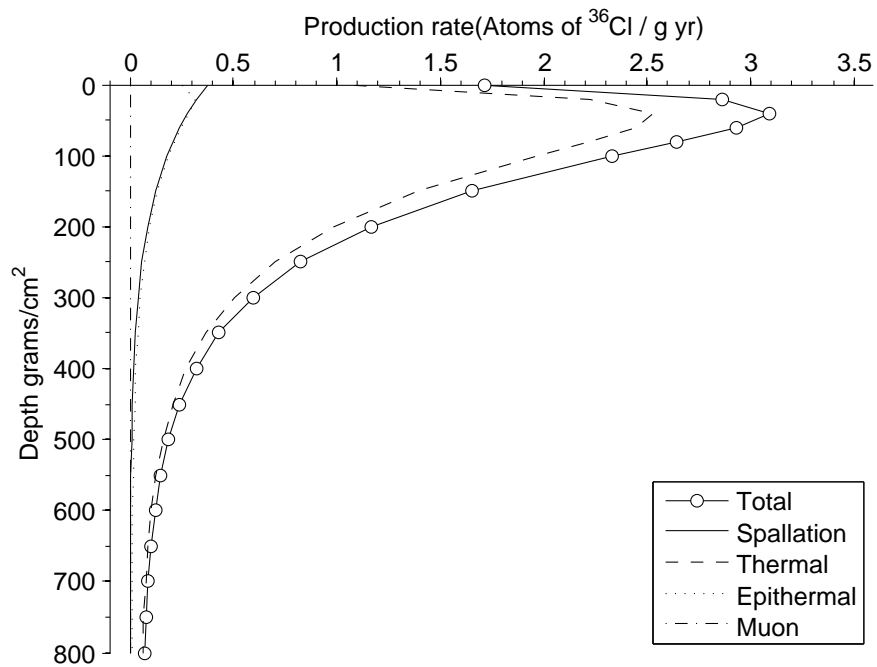


**Figure 2.6:** Relative Cl-36 production rates for the Copper Canyon calibration site. The composition of the surface sample was used to calculate the production rates with depth, of the various pathways. Thermal and epithermal production is approximately 50% of the total production.

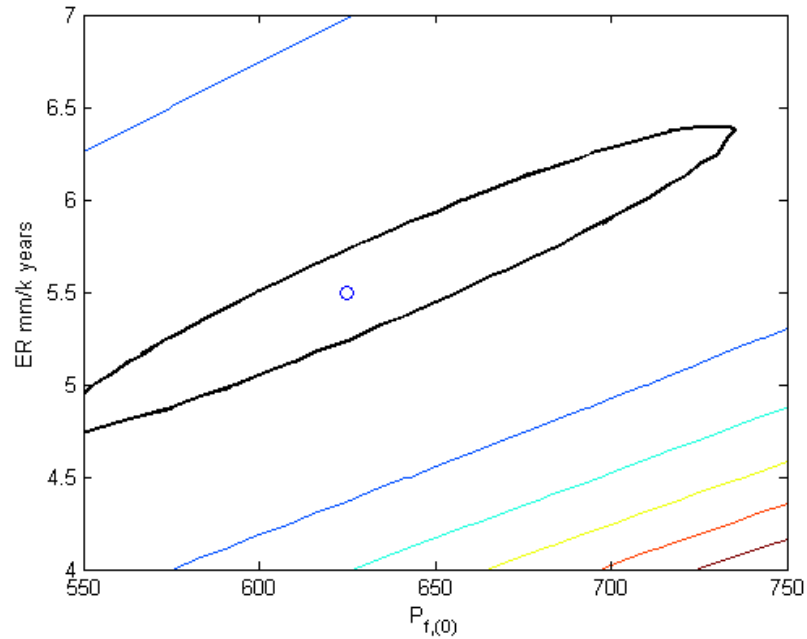


**Figure 2.7:** Production rate–erosion rate trade off. Shown are contours of the 2-dimensional  $\chi^2$  hyper-surface, used to evaluate the relationship between the fitted parameters.

## 2.2.4 Calibration

The Matlab function `syndatgen.m` was written to provide an easy way of quickly producing synthetic depth profiles, and was designed to be easily modified to replicate profiles from many different sites. First a series of inputs—erosion rate, age, and the appropriate level of concentration uncertainties must be set. For the synthetic calibration a 5% level of uncertainty was assigned to the concentrations to mimic the uncertainties reported to us by the AMS lab. The function then loads a vector of compositional data representing in this case, the Copper Canyon site. The compositions used to create the synthetic data was derived from preliminary sampling of the Copper Canyon site. Next `syndatgen.m` uses the  $^{36}\text{Cl}$  and  $^{10}\text{Be}/^{26}\text{Al}$  production models created by Borchers and Marrero to create depth profiles according to the given inputs. Outputted from the function are two profiles.

The first profile represents samples in which  $P_i(0)^{36}\text{Cl}$  is the dominant production pathway. The second is a representation of a  $P_{s,\text{SiO}_2}^{10}\text{Be}$  dominated profile. Normally distributed synthetic noise is added to both profiles at the prescribed uncertainty levels. `syndatgen.m` can then be called by a higher level Matlab script that actually does the calibration.

With synthetic data generated, the calibration begins within the MATLAB script `pf0dpcal.m`. We search for the minimum  $\chi^2$  solution through iterations of the Levenberg-Marquardt (LM) algorithm on equation 2.5.

$$\chi^2 = \sum_{i \in \text{depths}} \left( \frac{\text{ConcPred}(er, age)_i - \text{ConcSyn}_i}{\sigma_i} \right)^2 \quad (2.5)$$

A solution is returned once LM has converged to the minimum, within a tolerance of  $1.0\text{e-}4$ . Next we plot the minimum solution with  $1\text{-}\sigma$  and  $2\text{-}\sigma$  confidence regions, using the  $\Delta\chi^2$  method described in Bevington and Robinson (1969). That is, the approximate  $1\text{-}\sigma$  confidence region is bounded by the  $\chi^2$  hyper-surface contour equal to  $\chi_{min}^2 + \Delta^2$ , where  $\Delta^2 = \chi^2(0.68, df = 2)$  (Bevington and Robinson, 1969). Then we calculate the  $p\text{-value} = 1 - \chi^{-2}(\chi_{min}^2, df = 2)$ , where a  $p\text{-value} > \alpha$  signifies an acceptable fit at the  $100(1 - \alpha)\%$  confidence level<sup>1</sup>. The following section will include an examination of the results from our synthetic calibration. Furthermore, we will use the confidence region to determine if at all and by how much the precision of  $P_i(0)^{36}\text{Cl}$  could be increased by calibrating at Copper Canyon.

### 2.2.5 Results

Synthetic profiles were generated with an exposure age of 5000 k years and with 5% noise added to the concentrations of  $^{10}\text{Be}$  and  $^{36}\text{Cl}$ . Each profile contained

---

<sup>1</sup>Common values for  $\alpha$  are 0.05, 0.01.

11 depths with the top 7 equally spaced at 50 (g/cm<sup>2</sup>), and the lower 4 equally spaced at 100 (g/cm<sup>2</sup>)<sup>2</sup>. See figures 2.9 and 2.10. Constant compositions were used for both profiles, and initial values for erosion rate and P<sub>f</sub>(0)<sup>36</sup>Cl were 6.00 (mm/k years) and 700 respectively. The results of the synthetic calibration are summarized in table 2.1. Figure 2.8 shows a contour plot of the corresponding

P <sub>f</sub> (0) <sup>36</sup> Cl	677
Erosion rate	5.92
$\chi^2$	15.633
<i>p</i> -value	0.739

**Table 2.1:** Synthetic calibration results

$\chi^2$  hyper-surface. The minimum is marked with a circle, and a the 1 $\sigma$  confidence region is highlighted by the thick black line. Conservative intervals for the half widths for P<sub>f</sub>(0)<sup>36</sup>Cl and erosion rate can be taken from a sides of a box containing the entire confidence region. The half width for P<sub>f</sub>(0)<sup>36</sup>Cl is approximately 38 or about 5.5% of the simulated “true value”. This is considerably better than the previously published half width of 105 (16.8%). We can conclude from this experiment, that in the best case we may be able to improve the estimate of P<sub>f</sub>(0)<sup>36</sup>Cl by 3 fold. The next step will be to run the actual calibration with real data.

### 2.3 Actual Calibration

With the evidence from the synthetic calibration suggesting that calibration can work, we can go ahead and run the actual data. Table 2.2 contains a summary of the results. Figure 2.11 shows the resulting  $\chi^2$  hyper-surface has a single, clear and well behaved<sup>3</sup> minimum.

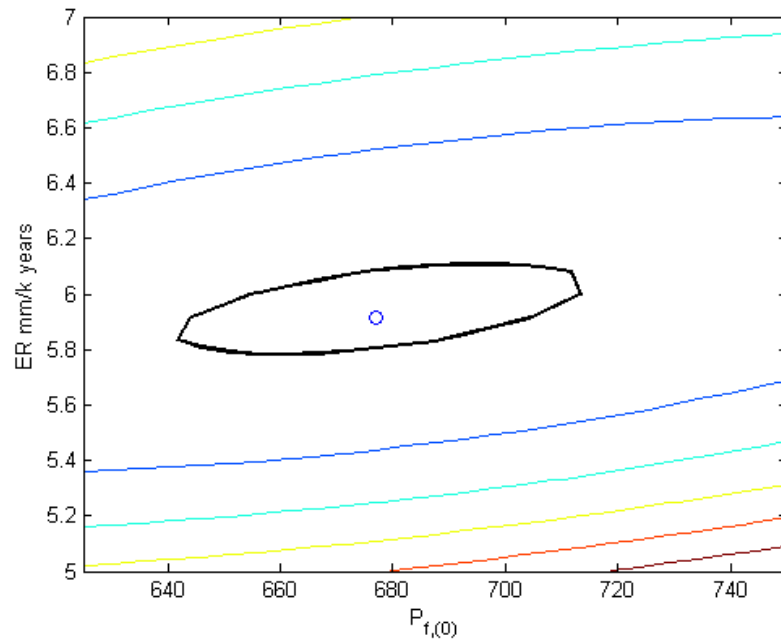


**Figure 2.8:**  $\chi^2$  hyper-surface of the synthetic calibration using a Be-10 spallation profile to constraint erosion rate

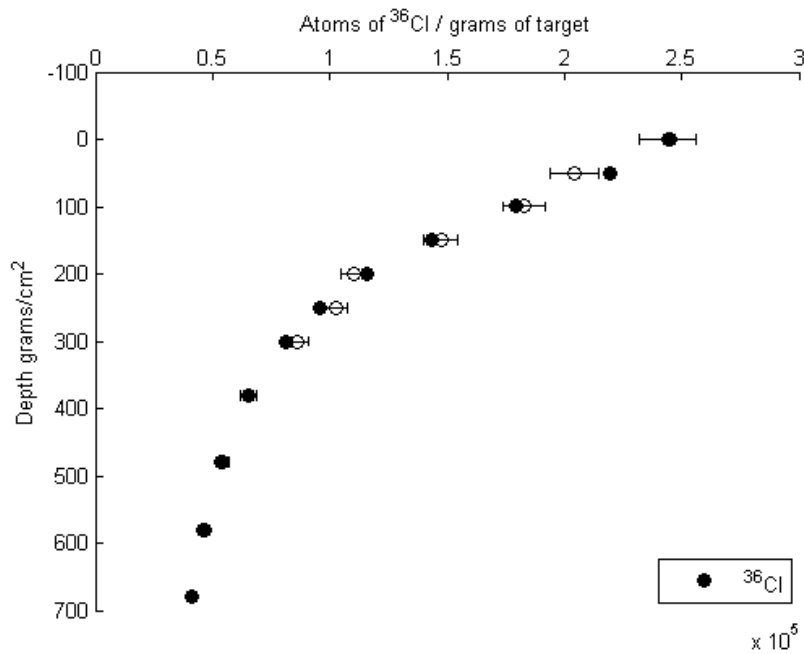


**Figure 2.9:** Synthetically calibrated chlorine-36 profile. The open circles represent the measured concentrations, while the filled in circles represent the predicted concentrations.

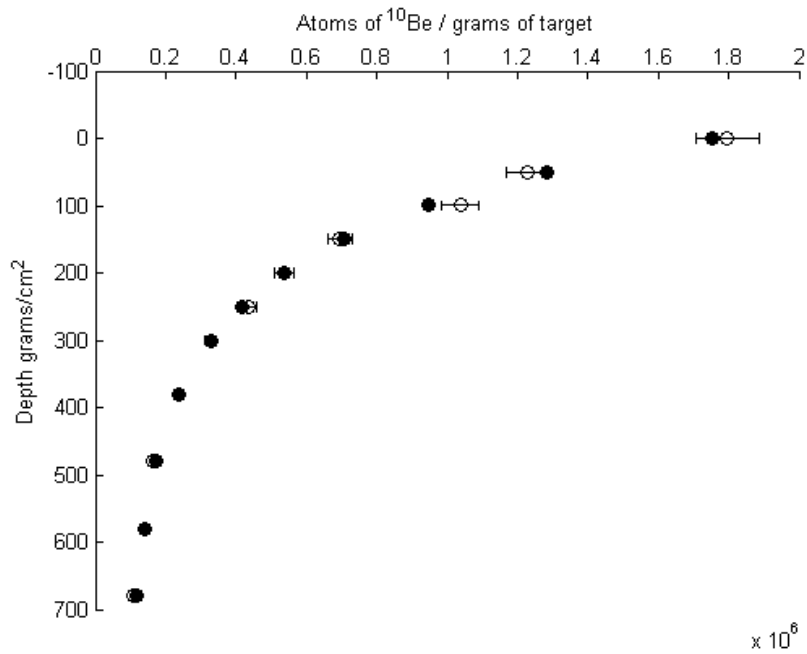


**Figure 2.10:** Synthetically calibrated beryllium-10 profile. The open circles represent the measured concentrations, while the filled in circles represent the predicted concentrations.

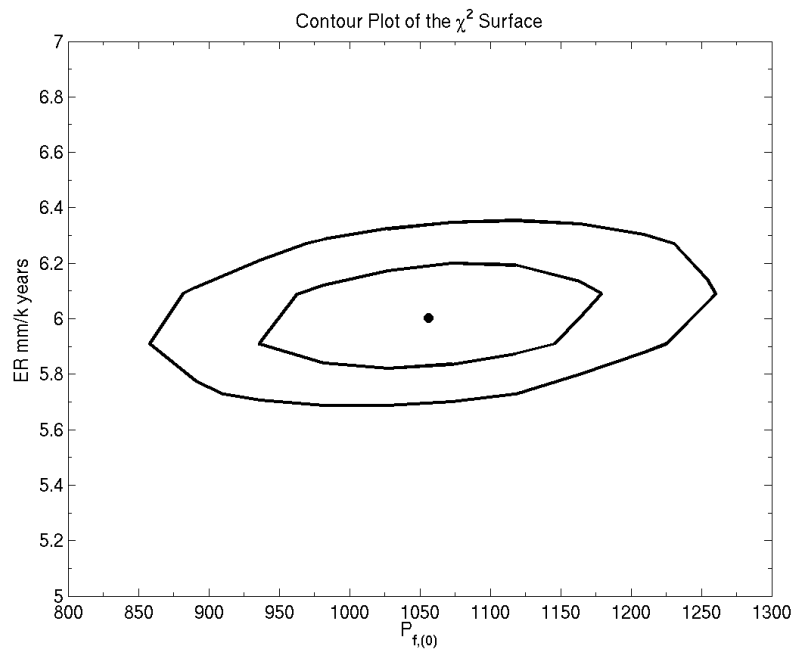


**Figure 2.11:** Calibration  $\chi^2$  hyper-surface

$P_f(0)^{36}\text{Cl}$	$1056.2 \pm 110 \text{ (n g}^{-1} \text{ yr}^{-1}\text{)}$
erosion rate	$6.00 \pm 0.20 \text{ (mm/ka)}$
$\chi^2$	20.566
<i>dof</i>	20
<i>p</i> -value	0.423

**Table 2.2:** Statistical summary of the calibration. Shown are the fitted parameters, and the meaningful statistics from the Copper Canyon calibration, using all samples.

Shown in figures 2.12 and 2.13, are the measured  $^{36}\text{Cl}$  and  $^{10}\text{Be}$  profiles. Both were plotted against the models predicted concentrations, using the best-fit parameters. It is clear that the  $^{10}\text{Be}$  profile fits the model well. The quality this fit is also reflected in the tight constraint on erosion rate, that is evident in figure 2.11. The  $^{36}\text{Cl}$  profile, however, is not as elegant. Of most concern, is the second to deepest sample in the profile. While the *p*-value suggests an appropriate fit to the data, figure 2.14 shows that second to deepest sample is greater than a  $3\text{-}\sigma$  outlier. To determine whether or not this is an influential outlier, the calibration was re-run without using the outlying sample. Table 2.3 lists the results from the experiment. While, having no effect on erosion rate,  $P_f(0)^{36}\text{Cl}$  increased approximately 8%. Additionally, the drastic increase in the *p*-value suggest that the fit has improved. However, after careful review of laboratory notes, Marrero (pers. comm, 2011) found no basis to remove the sample from the data set. Since the fit is still acceptable with all the data points, we will continue to use the full data set.

Another issue concerning the  $^{36}\text{Cl}$  profile are the large uncertainties on several of the data points. In fact, four of the samples have relative uncertainties of

---

<sup>2</sup>Spacing is approximately 20 cm and 40 cm respectively considering a density of  $2.6 \text{ g/cm}^3$

<sup>3</sup>The solution is well behaved, in the sense that the  $\chi^2$  hyper-surface is approximately elliptical near the minimum.

$P_i(0)^{36}\text{Cl}$	$1139.0 \pm 110$ ( $\text{n g}^{-1} \text{yr}^{-1}$ )
$\epsilon$	$6.00 \pm 0.20$ ( $\text{mm/ka}$ )
$\chi^2$	7.422
$dof$	19
$p$ -value	0.9916

**Table 2.3:** Statistical summary of the calibration. Shown are the fitted parameters, and the meaningful statistics from the Copper Canyon calibration, excluding the second to deepest samples.

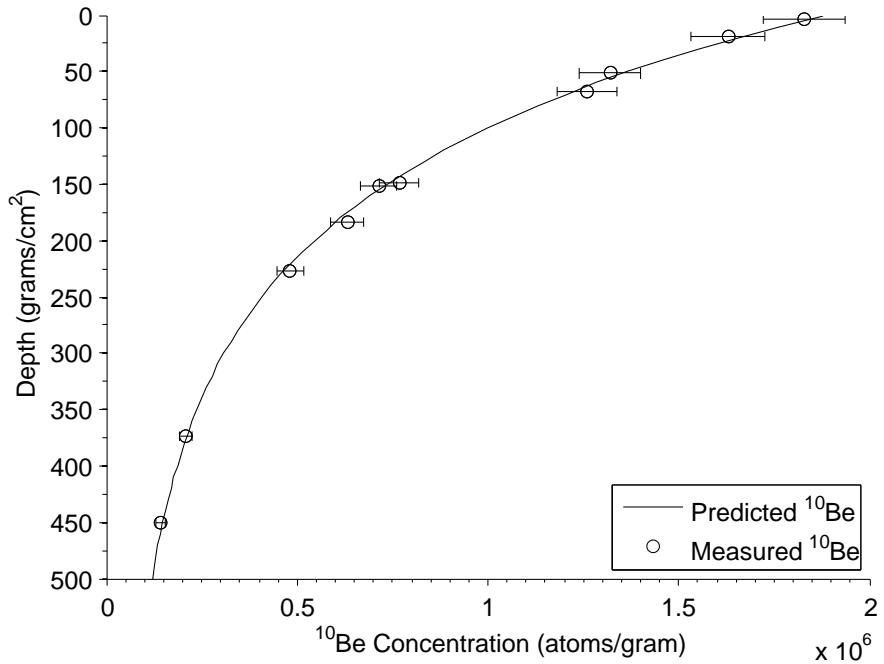


**Figure 2.12:** Calibrated beryllium-10 profile. Shown is the predicted beryllium profile vs the measured concentrations.

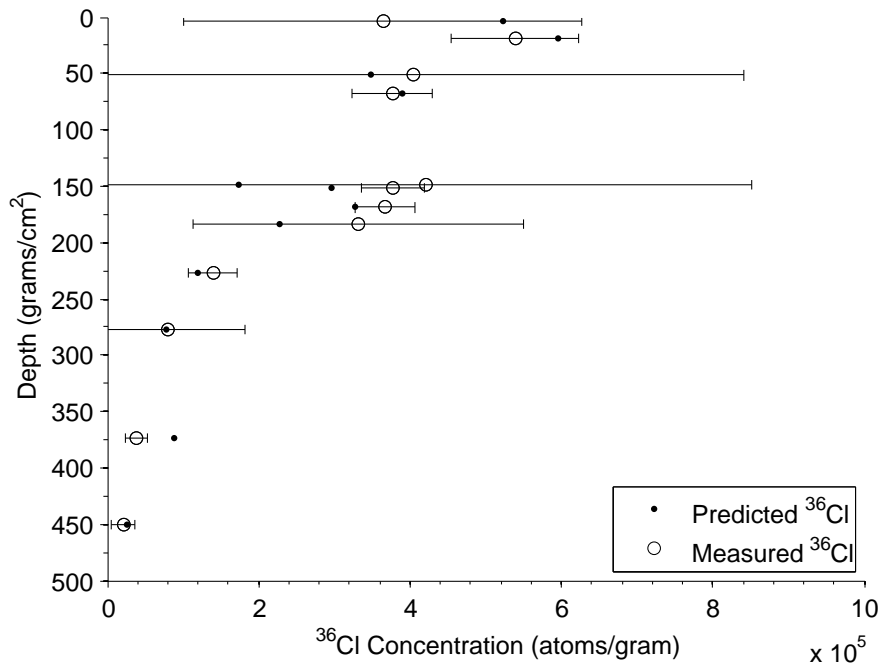


**Figure 2.13:** Calibrated chlorine-36 profile. Shows the predicted chlorine profile vs the measured concentrations. Since the concentrations vary sample-to-sample, the profile cannot be plotted as a continuous curve.

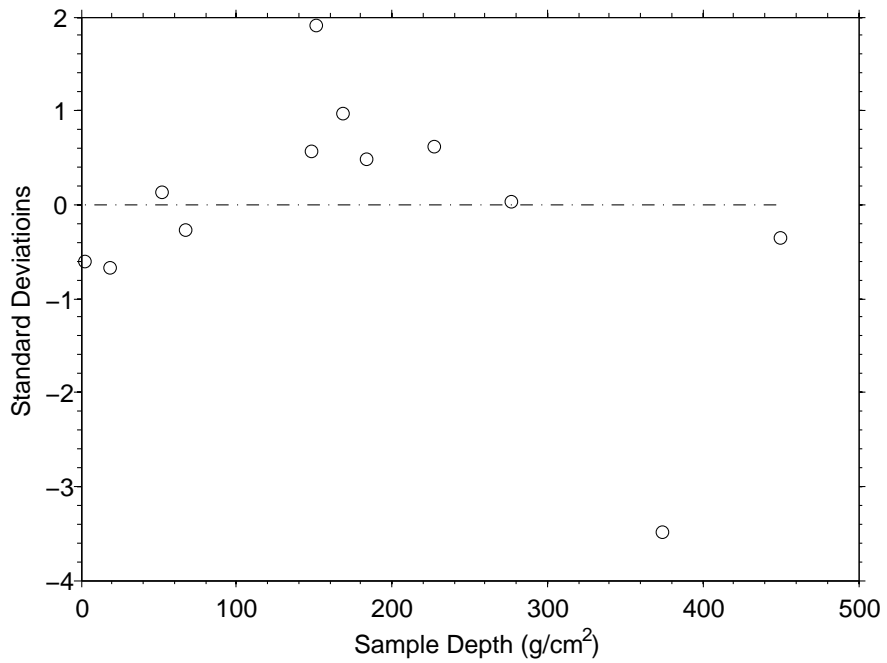


**Figure 2.14:** Standardized residuals plot. Shows the standardized residuals from 36-Cl profile.

more than 100%. Much of may be caused by the low concentrations of  $^{36}\text{Cl}$  in the samples. With low concentrations, the errors in the blank correction can be quite large relative to measured atom counts from the accelerator, thus leading to large uncertainties.

### 2.3.1 Calibration Summary

Through experiments with synthetic data, we first established the preferred site characteristics. Then, using the composition from the Copper Canyon site, we were able to determine that the best case scenario for the calibration could yield as much as a 3-fold decrease in the relative error of the estimate of  $P_i(0)^{36}\text{Cl}$ .

The results of the actual calibration give  $P_i(0)^{36}\text{Cl} = 1056.2 \pm 110 \text{ (n g}^{-1} \text{ yr}^{-1}\text{)}$ . The presence of a  $> 3\text{-}\sigma$  influential outlier was concerning, however, we found no laboratory evidence for the exclusion of the sample.

## CHAPTER 3

### DEPTH PROFILE CALCULATOR

#### 3.1 Bayesian Method

It was decided that the age calculation would be done as a Bayesian inverse problem. This approach has several advantages. First, unlike using a classical statistics approach to parameter estimation, the Bayesian approach treats unknown parameters as a random variables. Doing so allows us to report the resulting fitted parameters as expected values, accompanied by a probability distribution. Second, as will be described shortly, this approach also allows the user to submit prior information or expert knowledge, influencing the solver itself. However, this second advantage must also come with a warning. There is a dangerous game that can be played by using too influential a prior. One can easily and strongly bias the resulting posterior distribution with the selection of a informative<sup>1</sup> prior. One needs to carefully consider how sensitive an answer is to the prior distribution used, and responsibly report the effect that different priors have on their solution. Third, from a computational standpoint, the method presented in the next section is not susceptible to the convergence failures that iterative line search solvers can encounter in certain cases. Experience has shown that the age calculation problem is such a case. In the following paragraphs we describe in greater detail the methods used.

---

<sup>1</sup>The word informative is used to describe a distribution in which most to the probability is clustered over a relatively small range.

### 3.1.1 The Posterior Distribution

We'll start by introducing some notation. Let  $X$  be a random variable from the distribution  $f(x|\boldsymbol{\theta})$ , which is conditioned on the parameter vector  $\boldsymbol{\theta} = (\theta_1, \theta_2, \dots, \theta_p)$ . Since we are using a Bayesian approach we will also treat  $\boldsymbol{\theta}$  as a random quantity from the distribution  $\pi(\boldsymbol{\theta})$ . Now, suppose we have the sample  $\mathbf{x} = (x_1, x_2, \dots, x_n)$ . We could then calculate that sample's likelihood  $L(\mathbf{x}|\boldsymbol{\theta})$  as

$$L(\mathbf{x}|\boldsymbol{\theta}) = f(x_1|\boldsymbol{\theta})f(x_2|\boldsymbol{\theta}) \cdots f(x_n|\boldsymbol{\theta}). \quad (3.1)$$

The joint probability density of  $\mathbf{X}$  and  $\boldsymbol{\theta}$  is then

$$g(\mathbf{x}, \boldsymbol{\theta}) = L(\mathbf{x}|\boldsymbol{\theta})\pi(\boldsymbol{\theta}), \quad (3.2)$$

And the marginalized density of  $X$  is

$$g_{\mathbf{x}}(\mathbf{x}) = \int_{-\infty}^{\infty} g(\mathbf{x}, \boldsymbol{\theta})d\boldsymbol{\theta}. \quad (3.3)$$

Using Bayes formula, we can now define the posterior distribution, i.e. the distribution for  $\boldsymbol{\theta}$  conditioned by data  $\mathbf{x}$ , as

$$p(\boldsymbol{\theta}|\mathbf{x}) = \frac{g(\mathbf{x}, \boldsymbol{\theta})}{g_{\mathbf{x}}(\mathbf{x})} = \frac{L(\mathbf{x}|\boldsymbol{\theta})\pi(\boldsymbol{\theta})}{\int_{-\infty}^{\infty} L(\mathbf{x}|\boldsymbol{\theta})\pi(\boldsymbol{\theta})d\boldsymbol{\theta}}. \quad (3.4)$$

Generally the integral in the denominator can be hard to calculate if there are a large number of parameters. Alternatively, an algorithm like the Metropolis-Hastings sampler can be used to sample from the posterior. The beauty of Metropolis-Hastings is that you do not need to actually even compute the integral in the denominator. It works by constructing a Markov chain transition kernel  $q$ , with the corresponding invariant density  $p$ .  $q$  is constructed in just the right way so that samples from  $p$  are asymptotically distributed according to the posterior distribution. However, doing so creates statistically significant autocorrelation between

samples for even very large lags. Thus to insure independence, samples must be "thinned out", keeping only one every  $k$  consecutive samples. Often  $k$  needs to be as large as  $10^4$ . Therefore this method requires many iterations to obtain a enough samples to closely approximate the posterior distribution. The number of iterations needed increases by  $\mathcal{O}(m)$ , where  $m$  is number of estimated parameters. So for many large problems, as long as function evaluation are inexpensive, this solver can be highly useful. The Metropolis-Hastings algorithm is described in full detail within (Calvetti and Somersalo, 2007).

In our case with only three parameters to find, and relatively expensive function evaluations, Metropolis-Hastings is rather inefficient. In the next section we describe a more simplistic approach to find posterior distributions. It will rely on assuming normally distributed errors, but will allows us to analytically calculate the posterior distribution<sup>2</sup>.

This age calculator will be intended for public use by the global geoscience community. Therefore it must be made as user friendly as possible—which includes being expeditious. To avoid computation times rightly measured in hours, we decided to take different approach which has us directly calculate the posterior distributions. The 3 parameters to be estimated are *erosion rate*, *age*, and *inheritance*, or using the notation,  $\theta = (er, age, inher)$ . Let

$$x_i = p_i - c_i \tag{3.5}$$

be the difference between the measure concentration  $c_i$  and the predicted concentration  $p_i$ , at depth  $i$ . We assume that the residuals  $\mathbf{x}$  follow a normal distribution

---

<sup>2</sup>up to a scaling constant

with mean of zero and covariance matrix

$$\Sigma = \begin{pmatrix} \sigma_1 & 0 & \dots & 0 \\ 0 & \sigma_2 & \dots & 0 \\ \vdots & \vdots & \ddots & \vdots \\ 0 & 0 & \dots & \sigma_n \end{pmatrix}. \quad (3.6)$$

Then

$$f(x_i|\boldsymbol{\theta}) = \frac{1}{\sqrt{2\pi\sigma}} \exp\left(-\frac{x_i^2}{2\sigma_i^2}\right), \quad (3.7)$$

and the equation 3.1 becomes

$$L(\mathbf{x}|\boldsymbol{\theta}) = \prod_{i=1}^n \left(\frac{1}{\sqrt{2\pi\sigma_i}}\right) \cdot \exp\left(-\frac{1}{2} \sum_{i=1}^n \frac{x_i^2}{\sigma_i^2}\right). \quad (3.8)$$

Since we assumed  $\mathbf{x} \sim N(0, \sigma^2)$ <sup>3</sup>, then

$$\sum_{i=1}^n \frac{x_i^2}{\sigma^2} \sim \chi^2(n). \quad (3.9)$$

Equation 3.9 is an important result. It says that we can conveniently compute the likelihood surface by first calculating  $\chi^2$  values, and then transform them to a posterior using equations 3.8 and 3.4.

As for the denominator of equation 3.4, since we have only 3 parameters, the integration in the is relatively easy. A description of our computations are as follows: (i) Create an evenly spaced 3-dimensional<sup>4</sup> grid over the parameters of age, erosion rate and inheritance. (ii) Then, summing the contributions from each sample depth, we calculate  $\chi^2$  at each grid point according to equation 3.10.

$$\chi_{age,er,inher}^2 = \sum_i^n \left( \frac{ConcPred_{age,er,inher} - ConcMeas_i}{\sigma_i} \right)^2 \quad (3.10)$$

(iii) Next we transform the approximated  $\chi^2$  hyper-surface to a likelihood surface as in equation 3.8. We use a trapezoidal integration scheme to calculate

<sup>3</sup>The symbol  $\sim$  is read, "follows the distribution"

<sup>4</sup>Even spacing is consistent only within each dimension

the denominator, and are left with the joint posterior density  $p(\boldsymbol{\theta}|\mathbf{x})$ . Finally we marginalize  $p(\boldsymbol{\theta}|\mathbf{x})$  three times to get

$$\begin{aligned} p(er|\mathbf{x}) &= \int p(\boldsymbol{\theta}|\mathbf{x})d\theta_{age}d\theta_{inher} \\ p(age|\mathbf{x}) &= \int p(\boldsymbol{\theta}|\mathbf{x})d\theta_{er}d\theta_{inher} \\ p(inher|\mathbf{x}) &= \int p(\boldsymbol{\theta}|\mathbf{x})d\theta_{er}d\theta_{age}. \end{aligned}$$

Again we used a trapezoidal scheme to handle the integration.

More than simply knowing how each parameter is marginally distributed, it is important when assigning uncertainties, to determine if any multiple interactions exist between erosion rate, age and inheritance—we already expect there to be a trade off between erosion rate and age. To hunt for these interactions we create 3 pairwise 2-D contour plots of the joint posterior distribution. For example, if we integrate  $p(\boldsymbol{\theta}|\mathbf{x})$  over inheritance, we end up with the probability distribution

$$p(er, age|\mathbf{x}). \tag{3.11}$$

We can then plot contours representing 68% and 95% regions of probability. See figure 3.4. The contour that contains the desired probability is found by adding up all of the probability captured by a contour equal to  $\tau$ . We then iteratively adjust  $\tau$  either up or down by way of a bisection search.

### 3.1.2 Calculator Example

In this section we take a look at an example of the age calculator using CRONUS legacy data. At the present, versions of this calculator are available for  $^{10}\text{Be}/^{26}\text{Al}$  and  $^{36}\text{Cl}$ . We will show an example of our calculator, using a  $^{10}\text{Be}$  profile.

There should be no loss of generality, as the functionality is the same for any of the 6 common TCNs.

Our calculator produces seven plots. The first three are marginal posterior distributions for each of erosion rate, age, and inheritance. Next we produce pairwise contour plots of the likelihood surface for each pair of the estimated parameters. In each contour plot the 3rd parameter has been integrated out of the likelihood surface. Lastly, we produce a plot of the predicted versus measured concentrations, complete with  $1-\sigma$  error bars.

**Greenland** The Scoresby Sund region, located in eastern Greenland contains well constrained late Holocene moraine deposits (Goehring et al., 2010). One of these deposits, an ice-contact delta, was sampled at 3 locations for depth profiles. Additionally 7 glacial boulders were sampled, and all were processed for  $^{10}\text{Be}$  by Goehring et al. A detailed description of sampling methods and site characteristics can be found in the reference (Goehring et al., 2010).

The best profile in terms of  $\chi^2$  goodness of fit (IC06-3), was chosen from Goehring et al. Comparing our results to Goehring's offer us a check on the reasonableness of our calculations. Uniform priors were used for all 3 parameters.

Figures 3.1, 3.2, and 3.3 show the marginal posteriors for erosion rate, age and inheritance. While the age and inheritance distributions are nicely bell shaped, the distribution of possible erosion rates is essentially flat, and reaches a sharp cut off at rates just below negative one<sup>5</sup>. This result can be explained by the following example. Suppose you have a depth profile that was exposed 100k

---

<sup>5</sup>Negative erosion rates are to be interpreted as post exposure accumulation, such as sedimentation

years ago. Now suppose that the shallowest sample in the profile is at 50 mm. It would then be impossible for there to have been more than 2 mm per thousand years of accumulation.

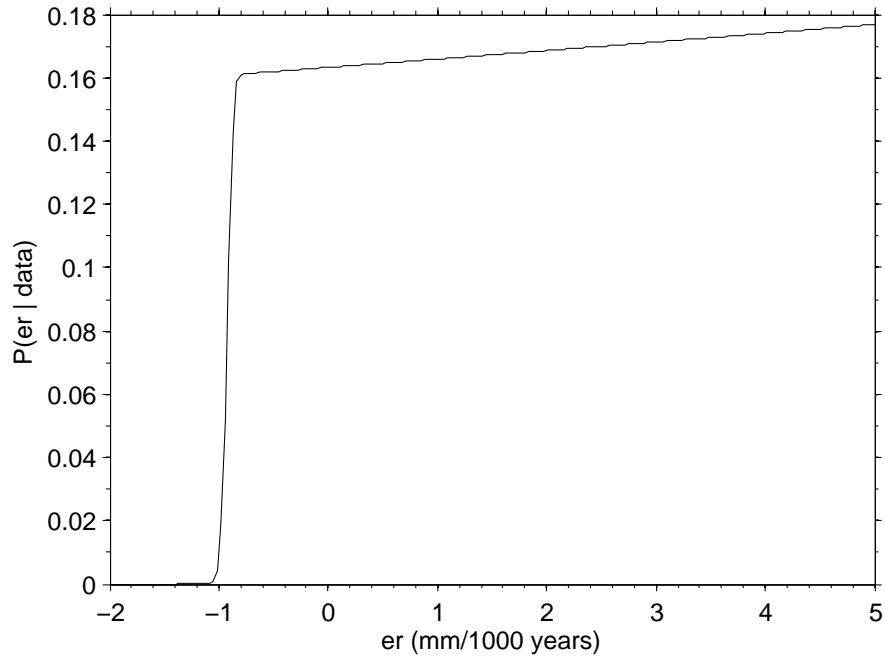


**Figure 3.1:** Marginal distribution for erosion (Greenland IC06-3 profile).

Next we'll discuss the pairwise contour plots. Figure 3.4 shows the relationship between erosion rate and age. In the Greenland profile the erosion rate is only constrained by the impossibility of less than -1 mm/ka of erosion (accumulation). This may seem to contradict statements in the calibration section, where a  $^{10}\text{Be}$  profile was used to tightly constrain the erosion rate. Because the Greenland profile was not at concentration equilibrium, the extra degrees of freedom provided by needing to fit the age and inheritance, make it impossible to discern any information about the erosion rate. On the other hand, the equalized "old" profile with no inheritance, had only a single free parameter—erosion rate.

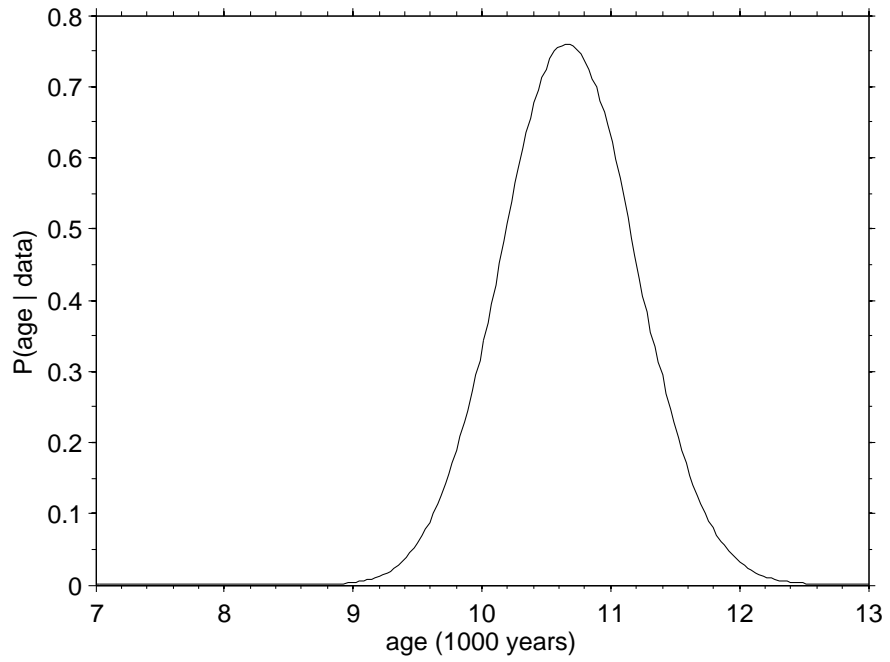


Figure 3.2: Marginal distribution for age (Greenland IC06-3 profile).

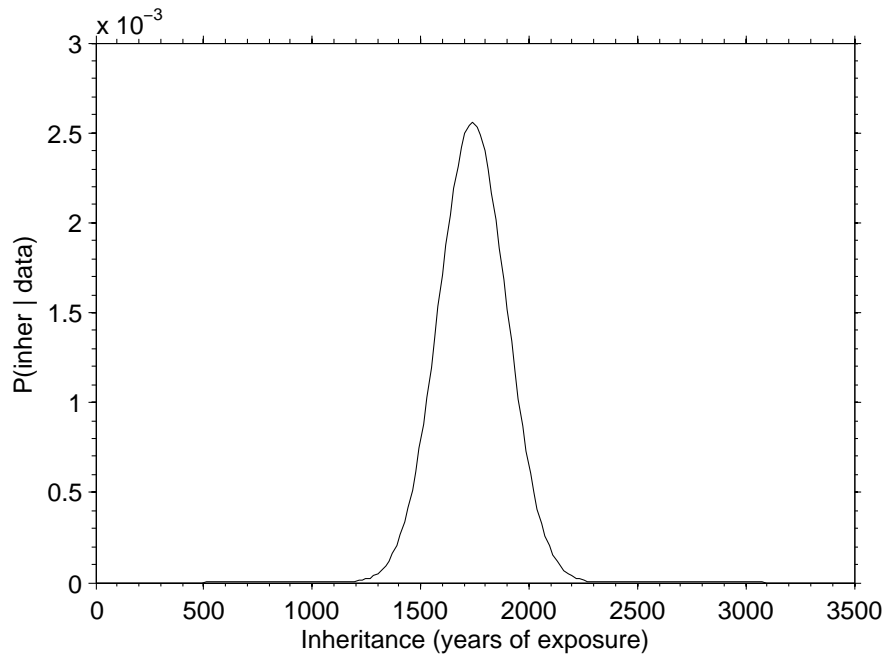
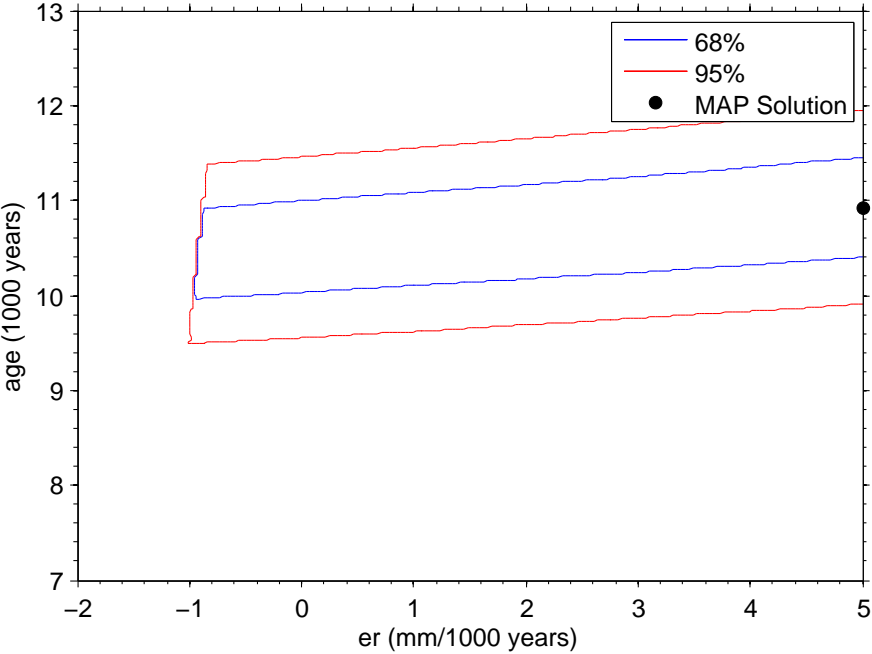


Figure 3.3: Marginal distribution for inheritance (Greenland IC06-3 profile).

We can see in figure 3.5 that there appears to be significant correlation between estimating the age and inheritance of a sample. Similar to the relationship between age and erosion rate, figure 3.6 shows no interaction between erosion rate and inheritance.



**Figure 3.4:** Joint posterior marginalized over inheritance (Greenland IC06-3 profile).

We can now assign some uncertainties to our estimated parameters. Keep in mind however, that the uncertainties presented here are not the classic frequentest confidence intervals. Instead, we present the maximum a posterior solution (MAP), coupled with a distribution of probability for each parameter. In other words, most likely (in the probabilistic sense) combination of erosion rate, age, and inheritance, given the data and the prior distributions we assigned. The MAP solution to the Greenland profile is provided in table 3.1 along with 68 percent probability bounds taken from the most conservative boundaries from the pairwise contour plots. Also listed in 3.1 are the estimates from Goehring et al.,

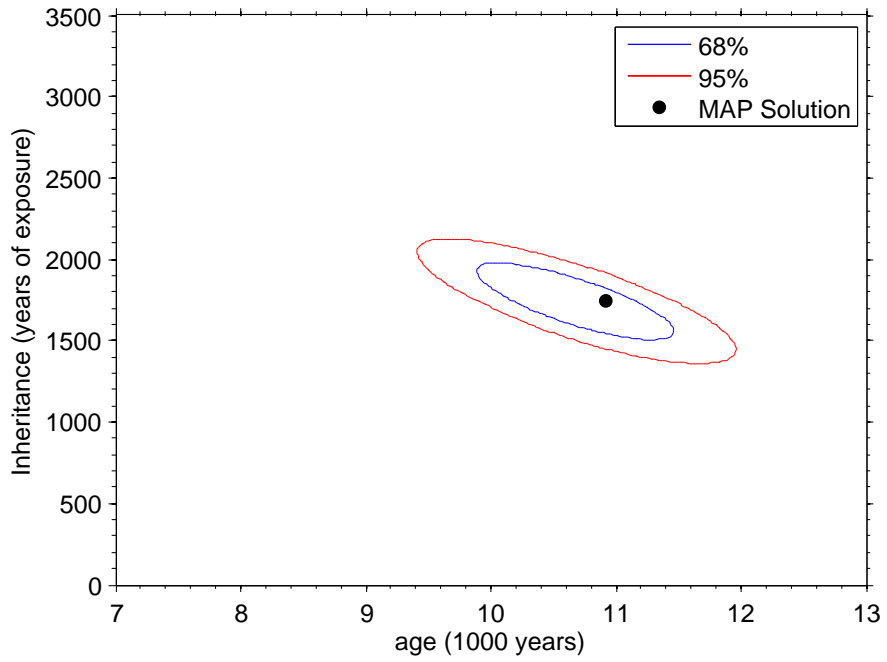


**Figure 3.5:** Joint posterior marginalized over erosion rate (Greenland IC06-3 profile).

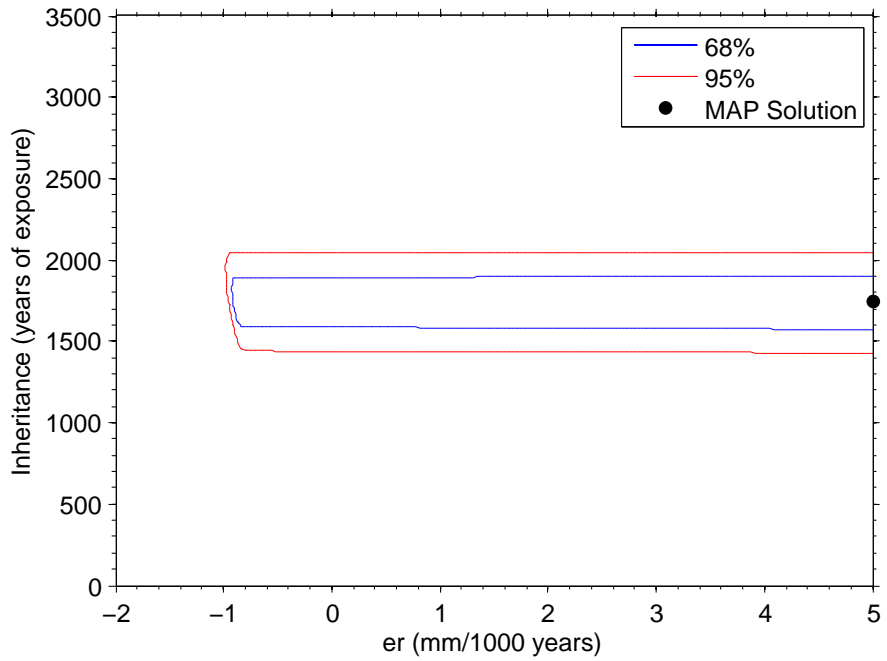


**Figure 3.6:** Joint posterior marginalized over age (Greenland IC06-3 profile).

with frequentist 68% confidence intervals. Goehring's erosion rate is starred to denote that it was assumed to equal zero, and was not fitted with the data.

We see that our results are well within the uncertainties of Goehring's. Differences between our models easily explain any differences between our results. First, and most important, our models of production are quite different. Goehring uses the relatively simple model shown in equation 3.12,

$$N(z) = N_{inher}(z) + N_{surf}(z) \exp\left(\frac{-z}{\Lambda_{spall}}\right), \quad (3.12)$$

where  $z$  is the depth in grams/cm<sup>2</sup>,  $N_{inher}$  is the inheritance at depth  $z$ ,  $N_{surf}$  is the surface nuclide concentration since deposition, and  $\Lambda_{spall}$  is the spallation attenuation length (Goehring et al., 2010). Since this model is only valid for the case of zero erosion, a zero erosion rate was assumed. In contrast, our numerical model not only allows for non zero erosion rates, but more importantly also has production from muons, where Goehring assumes production is solely from spallation. Second, we used a slightly different production rate for <sup>10</sup>Be. While we used a newly calibrated 4.22 atoms/gram/year, Goehring et al. uses 4.41 atoms/gram/year, calibrated by Balco et al. Third, while we used Lifton/Sato scaling, Goehring uses Dunai (2000). Lastly, unlike Goehring, we fit erosion rate simultaneously with age and inheritance. Taken all together, that fact the our results did not exactly match the values presented in Goehring et al., is not surprising in the least. We can, however, still use the comparison to check for reasonableness.

Lastly, we have the measured concentrations plotted against the predicted concentrations produced by our model. See figure 3.7. Also shown, are the reported one sigma error bars upon the measured concentrations. It appears that

Profile	Parameter	Our Results	68% BCI	Goehring et al.
IC06-3	Erosion Rate (mm/ka)	5.00	[-0.96, 5.00]	0*
IC06-3	Age (ka)	10.92	[9.90, 11.45]	11.08 ± 0.43
IC06-3	Inheritance (ka)	1.57	[1.51, 1.98]	1.39 ± 1.20

**Table 3.1:** Greenland Results. Shown above, is a comparison of the estimated parameters between our depth profile calculator and Goehring et al. The \* next to Goehring’s erosion rate denotes that a fixed value was used.

Depth	Uncertainty (%)
0	5.0
48.25	5.9
96.35	3.1
193.00	3.8
272.66	4.0

**Table 3.2:** Relative uncertainties for the Greenland IC06-3 profile.

there may be some systematic misfit to the profile. The deeper samples were generally under estimated, while the shallower samples have been over estimated. Figure 3.8 shows the same profile recalculated with a upper bound of zero erosion rate. Although only slightly, by lowering the maximum erosion rate allowed, the predicted concentrations near the top are pulled back closer to the what was measured. This may seem counter-intuitive, however, an explanation can be found in the relative uncertainties. Table 3.2 shows the relative uncertainties in the Greenland profile.

By allowing a higher erosion rate, you can obtain a slightly better fit, by closely fitting the deep (more accurate samples), at the expense of misfitting the near surface samples (less accurate samples). While these changes in fit are minor, it still shows the importance that constraining the maximum erosion rate has to the fitted profile.

Alternatively, it is likely that good fit could be gotten at any erosion rate,

if we simultaneously fit attenuation length. This is undesirable for at least 2 reasons. First, adding a 4th parameter takes away a degree of freedom, and thus increases the number of depth samples needed to maintain that  $n_{pars} < n_{data}$ . Second, since improving the fit can be achieved by adjusting the erosion rate or (likely) the attenuation length, it is nearly certain that erosion rate and attenuation length will be highly correlated. The result of this, will be the subsequent inflation of the correlated parameters. The net effect is that the uncertainty in the age estimate will be further degraded.

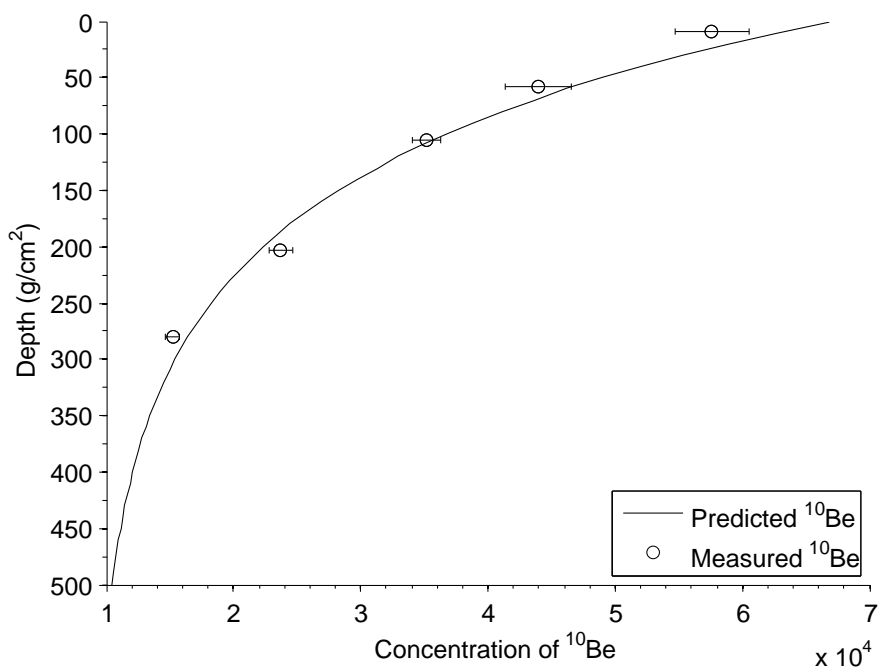


**Figure 3.7:** Greenland profile. Shown is the IC06-3 Greenland profile corresponding to figures 3.1 - 3.6.

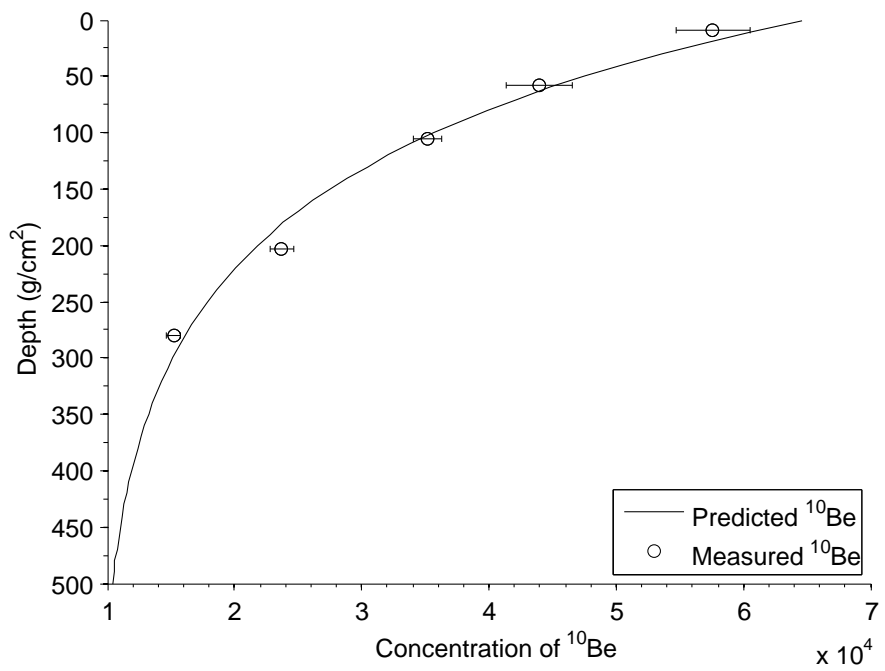


**Figure 3.8:** Greenland profile. Shown is the IC06-3 Greenland profile fitted with a reduced range of erosion rates; -2 mm/ka to 0 mm/ka

## CHAPTER 4

### SUMMARY AND CONCLUSIONS

After introducing TCN dating methodology in the first chapter, in chapter two we presented our methodology for calibrating the production rate parameter  $P_i(0)^{36}\text{Cl}$ , for thermal and epithermal production energies. It was determined by synthetic experimentation that a site should be both “old enough” to have reached profile equilibrium, and ideally have a low erosion rate. With a lower erosion rate we retain the hook in the depth curve, thus preserving more information about the  $^{36}\text{Cl}$  production. The site should also have a composition such that the dominant production is from thermal and epithermal pathways, and be lacking or completely void of production from spallation and muons. We showed that the Copper Canyon site was reasonably suitable for proper calibration. While the erosion rate was initially unknown it was believed to be relatively low ( $< 5\text{mm/k years}$ ), and the age of the site to be extremely old ( $> 2000\text{ k years}$ ). The initial exercise examining the composition showed the production profile would be thermally and epithermally dominated (91.5%).

Next we did further synthetic experimentation to lay down upper bounds on the quality of the calibration. Depths were created ranging from the surface to  $700\text{ g/cm}^2$ , and using a composition matching that of the surface sample, we ran the forward production model to create concentrations. After adding 5% noise to the synthetic concentrations, we inverted the model, and calculated the uncertainty on the parameters of  $P_i(0)^{36}\text{Cl}$  and erosion rate. First we inverted using only

the chloride profile. This produced best case confidence intervals of  $\pm 16.8\%$ —no better than the previous estimate of  $626 \pm 105$ . See figure 2.7. Thus it was decided to use  $^{10}\text{Be}$  depth profile in addition to the  $^{36}\text{Cl}$  profile, to tie down the erosion rate, and improve the estimate of  $P_f(0)^{36}\text{Cl}$ . Figure 2.8 shows the improvement in half width from 16.8% to 5.5%, that was obtained by using the  $^{10}\text{Be}$  profile.

Proceeding with the actual calibration, we were able to obtain a statistically acceptable fit using all<sup>1</sup> of the data from the Copper Canyon profile. The uncertainties on the measured concentrations were found to be quite high. This may suggest that future work may be able to improve the estimated  $P_f(0)^{36}\text{Cl}$ , by finding a depth profile with more accurate concentrations.

Chapter 3 developed our approach to the Bayesian inverse problem—the depth profile age calculator. We evaluated the sum of squares misfit over a 3-dimensional grid, and use likelihoods to transform the surface into a joint posterior distribution of the parameters age, erosion rate, and inheritance. As an example of its' functionality, and to avoid problems with an uncalibrated  $P_f(0)^{36}\text{Cl}$ , we used the calculator to date a  $^{10}\text{Be}$  profile from Greenland taken from Goehring et al. (2010). It was shown that the dates produced by our calculator were in reasonable agreement with the independently published values in Goehring et al.

---

<sup>1</sup>Including the influential outlier

## REFERENCES

- Balco, G., Stone, J. O., Lifton, N. A., and Dunai, T. J. (2008). A complete and easily accessible means of calculating surface exposure ages or erosion rates from  $^{10}\text{Be}$  and  $^{26}\text{Al}$  measurements. *Quaternary Geochronology*, 3:174-195.
- Bevington, P. R. and Robinson, D. K. (1969). *Data reduction and error analysis for the physical sciences*. McGraw-Hill New York.
- Calvetti, D. and Somersalo, E. (2007). *Introduction to Bayesian scientific computing: ten lectures on subjective computing*. Springer Verlag.
- Desilets, D., Zreda, M., Almasi, P., and Elmore, D. (2006a). Determination of cosmogenic  $^{36}\text{Cl}$  in rocks by isotope dilution: innovations, validation and error propagation. *Chemical geology*, 233(3-4):185-195.
- Desilets, D., Zreda, M., and Prabu, T. (2006b). Extended scaling factors for in situ cosmogenic nuclides: New measurements at low latitude. *Earth and Planetary Science Letters*, 246(3-4):265-276.
- Dunai, T. (2001). Influence of secular variation of the geomagnetic field on production rates of in situ produced cosmogenic nuclides. *Earth and Planetary Science Letters*, 193(1-2):197-212.
- Dunai, T. J. (2010). *Cosmogenic Nuclides. Principles, Concepts and Application in the Earth Surface Sciences*. Cambridge University Press, UK.
- Evans, J. (2001). *Calibration of the production rates of cosmogenic  $^{36}\text{Cl}$  from potassium*. PhD thesis, Australian National University.
- Goehring, B., Kelly, M., Schaefer, J., Finkel, R., and Lowell, T. (2010). Dating of raised marine and lacustrine deposits in east Greenland using beryllium-10 depth profiles and implications for estimates of subglacial erosion. *Journal of Quaternary Science*, 25(6):865-874.
- Gosse, J. C. and Phillips, F. M. (2001). Terrestrial in situ cosmogenic nuclides: theory and application. *Quaternary Science Reviews*, 20(14):1475-1560.
- Heisinger, B., Lal, D., Jull, A. J. T., Kubik, P., Ivy-Ochs, S., Neumaier, S., Knie, K., Lazarev, V., and Nolte, E. (2002). Production of selected cosmogenic radionuclides by muons: 1. fast muons. *Earth and Planetary Science Letters*, 200(3-4):345-355.

- Hidy, A., Gosse, J., Pederson, J., Mattern, J., and Finkel, R. (2010). A geologically constrained monte carlo approach to modeling exposure ages from profiles of cosmogenic nuclides: An example from lees ferry, arizona. *Geochem. Geophys. Geosyst*, 11:Q0AA10.
- Lal, D. (1991). Cosmic ray labeling of erosion surfaces: in situ nuclide production rates and erosion models. *Earth and Planetary Science Letters*, 104(2-4):424–439.
- Lifton, N., Bieber, J., Clem, J., Duldig, M., Evenson, P., Humble, J., and Pyle, R. (2005). Addressing solar modulation and long-term uncertainties in scaling secondary cosmic rays for in situ cosmogenic nuclide applications. *Earth and Planetary Science Letters*, 239(1-2):140–161.
- Marrero, S. M. (2009). Chlorine-36 production rate calibration using shorelines from pleistocene lake bonneville. Master's thesis, New Mexico Institute of Mining and Technology.
- Nishiizumi, K., Kohl, C., Winterer, E., Klein, J., Middleton, R., and Arnold, J. (1989). Cosmic ray production rates of Be-10 and Al-26 in quartz from glacially polished rocks. *Journal of Geophysical Research*, 94(B12):17907–17915.
- Phillips, F. M., Stone, W. D., and Fabryka-Martin, J. T. (2001). An improved approach to calculating low-energy cosmic-ray neutron fluxes near the land/atmosphere interface. *Chemical Geology*, 175(3-4):689–701.
- Sato, T. and Niita, K. (2006). Analytical functions to predict cosmic-ray neutron spectra in the atmosphere. *Radiation research*, 166(3):544–555.
- Sato, T., Yasuda, H., Niita, K., Endo, A., and Sihver, L. (2008). Development of PARMA: PHITS-based analytical radiation model in the atmosphere. *Radiation research*, 170(2):244–259.
- Swanson, T. and Caffee, M. (2001). Determination of  $^{36}\text{Cl}$  production rates derived from the well-dated deglaciation surfaces of Whidbey and Fidalgo Islands, Washington. *Quaternary Research*, 56(3):366–382.